# Rheological behaviour of low-heat Portland cement paste with MgO-based expansive agent and shrinkage reducing admixture

Shenghao Zuo [a], Qiang Yuan [a,*], Tingjie Huang [a], Mingzhong Zhang [b], Qihong Wu [c]

[a] *School of Civil Engineering, National Engineering Laboratory for High Speed Railway Construction, Central South University, Changsha 410075, China*

[b] *Department of Civil, Environmental and Geomatic Engineering, University College London, London WC1E 6BT, UK*

[c] *School of Architecture and Civil Engineering, Chengdu University, Chengdu 610106, China*

**Abstract:** The combined use of low heat Portland cement (LHC), MgO-based expansive agent (MEA) and shrinkage reducing admixture (SRA) is beneficial to reduce the cracking risk of concrete. In this study, the effects of MEA and SRA on the rheological behaviour of LHC paste were investigated using dynamic and static shearing tests. The response surface methodology was used to estimate the effects of MEA, SRA, and superplasticizer on dynamic rheological parameters, while the zeta potential, calorimetric, and solid phases tests were conducted to explore the mechanisms of time-dependent rheological behaviour. Results indicate that MEA contributes to higher dynamic yield stress and plastic viscosity, while the effect of SRA is dependent on its dosage. MEA promotes the static yield stress development for accelerating the hydration of blends and the formation of $Mg(OH)_2$. SRA retards the hydration of LHC and blended paste and reduces the number of main hydration products. However, the static yield stress is further increased by SRA, showing a consistent changing trend with the surface area of hydrated particles.

***Keywords:*** Magnesium oxide; Rheology; Yield stress; Plastic viscosity; Microstructure

## 1 Introduction

Cracks induced by constraint shrinkage [1] are of great concern to the durability of concrete. Recently, anti-crack concrete was regarded as a crucial field for the construction industry in China [2] and multiple approaches have been required to minimise non-structural cracks [3]. In Southwest China, the low heat Portland cement (LHC) [4] and reactive MgO [5] have been widely used to control the cracks in hydraulic concrete infrastructures. The use of shrinkage reducing admixture (SRA) is an emerging measure on inhibiting both autogenous and drying shrinkages of concrete [6]. As the

* Corresponding author. Email address: yuanqiang@csu.edu.cn (Q. Yuan)

conventional measures cannot mitigate the all-stage shrinkage of concrete, in recent years researchers attempt to use a combination of multifunctional admixtures to control concrete cracking and found the combined use of LHC, MgO-based expansive agent (MEA), and SRA has the potential to produce low even zero shrinkage concrete and thus can meet the requirements for practical applications [7-9].

LHC is a kind of cement with low hydration heat and low $CO_2$ emission [2]. The main clinker components and hydration products of LHC are similar to that of ordinary Portland cement (OPC), but the hydration rate of LHC is much lower because of its higher content of $C_2S$ and lower content of $C_3S$ in comparison with OPC [10, 11]. Moreover, the calcination temperature of LHC is about 1250-1350 °C, which is 100-200 °C lower than that of OPC. Compared to OPC, LHC contains less $CaCO_3$ in terms of raw materials, thereby resulting in lower environmental impact [11]. The use of LHC for the massive concrete can help reduce the internal accumulated heat and thermal gradient and thus mitigate the temperature-induced cracks in concrete structures [2].

SRA has been used in modern concrete to mitigate shrinkage, especially for autogenous shrinkage [4]. The SRA molecule usually has a hydrophilic head and a hydrophobic tail. The dispersed SRA molecules in the pore solution adsorb on the solution-solid and solution-air interfaces in cement paste and reduce the interfacial energy of solid particles as well as the surface tension of the pore solution [4]. As a result, SRA can effectively reduce autogenous shrinkage and drying shrinkage. In most cases, SRA is simultaneously used along with polycarboxylate ether-type superplasticizer (SP) in modern concrete where SP mainly works by adsorbing on the solution-solid interface [12]. In fresh cement suspensions, adsorptions of SRA and SP are crucial for their functions, which are generally characterized by UV-visible absorption spectrum [13], zeta potential [14], and total organic carbon tests [14, 15]. The competitive adsorption between SP and retarder was reported by Plank et al. [16], whereas the interaction of SRA and SP molecules which may affect the behaviour of fresh cement paste has not been fully understood.

MEA is a widely used expansive agent in China because of its low water demand and independence of curing regime [3]. In blends of cement and MEA, the formation of brucite, i.e. $Mg(OH)_2$, compensates the shrinkage of concrete. Moreover, the reaction process of MEA can be controlled by changing the calcination temperature [3]. The combined use of SRA and expansive agents more effectively compensate for the shrinkage of concrete [17-19], which is attributed to the retarding effect of SRA on cement hydration [20-22] and the refinement of hydration products [20-22].

Rheological properties are crucial to the workability of cement-based materials, which can be affected by the constituents [24], interparticle interactions [25, 26], and chemical additives [27-29]. The addition of MEA is reported to significantly decrease the flowability of fresh cement paste [30-32] as MEA aggravates the agglomeration of particles [30], while the effect of SRA on the workability of concrete is still controversial [33, 34]. Besides, the mineral compositions of LHC are different from that of OPC, thereby altering the surface charge of particles which is an important parameter affecting the flowability of fresh paste. As a result, the mixtures with LHC, SRA, and MEA may lead to different rheological properties in comparison with normal concrete, which notably influences the concrete transportation and casting processes in practice. The rheological behaviour of cement paste exhibits a time-dependent feature and is highly associated with the formation of CSH at the early age [35], suggesting that the lower alite content and hydration rate of LHC would lead to a relatively lower CSH content as well as different rheological behaviour from OPC. When LHC is used together with MEA and SRA, the rheological properties of cement paste would be much more complicated due to their interactions. It is vital to investigate the rheological behaviour and early-age hydration of LHC containing MEA and SRA for its widespread application, which have not been extensively addressed.

The main purpose of this paper is to investigate the combined effect of MEA, SRA, and SP on the rheological behaviour of LHC paste using dynamic and static shearing tests. Firstly, the individual and combined effects of SRA (0, 1.5%, 2%, and 2.5%), MEA (0, 8%, 10%, and 12%), and SP (0.2%, 0.3%, and 0.4%) on the dynamic yield stress and plastic viscosity were estimated by fitting the shear stress-shear rate curve with Bingham model as per the response surface methodology [36] that is an effective statistical approach for multi-variable problems. Then, the interactions between SRA and SP in fresh mixtures of LHC and MEA were explored using zeta potential tests. Besides, the static shearing test, calorimetric test, zeta potential test, X-ray diffraction (XRD), Thermogravimetric analysis (TGA), and scanning electron microscopy (SEM) were conducted on hydrated blends to study the static yield stress development. Finally, the hydration process, solid phases, and microstructure of mixtures in the period of 0-2 h were discussed in detail to fully understand the mechanism behind the time-dependent behaviour. The work may provide some insight into the design of anti-crack concrete from the rheological perspective.

## 2 Experimental program

### 2.1 Raw materials

Commercial LHC from Leshan, China complied with Chinese standard GB/T 200-2017 [37] and MEA from Nanjing, China complied with Chinese standard T/CECS 540-2018 [38] were used in this study. The average particle size and apparent density of LHC are 17.10 μm and 3.19 g/cm$^3$, respectively. The average particle size and apparent density of MEA are 32.83 μm and 2.98 g/cm$^3$ respectively, the reactivity of MEA, as characterized by the citric acid neutralization method [30, 31], is 153 s. Table 1 presents the chemical and mineral compositions of LHC and MEA, which are determined by X-ray fluorescence and Quantitative XRD tests respectively. The particle size distribution curves are shown in Fig. 1a. Polyether-type SRA with the appearance of a clear liquid was used. The function groups obtained by Fourier transform infrared spectroscopy are shown in Fig. 1b. The characteristic peak of C-O in ethers is observed at a wavenumber of 1105.44 cm$^{-1}$, while the characteristic peaks in the range of 2931.31 cm$^{-1}$ and 2973.80 cm$^{-1}$ are stemmed from the saturated hydrocarbon and the characteristic peak at 2973.80 cm$^{-1}$ corresponds to the hydroxyl. Then the $^1$H NMR analyse of SRA by dissolving in deuteroxide ($D_2O$) was conducted on BRUKER AVANCE III HD 400 MHz, as shown in Fig. 1c, the simplified molecular formula of SRA is also given. Polycarboxylate ether-type SP with a conventional comb-type structure was used, the solid content of SP is 20%.

Table 1 Chemical and mineral compositions of LHC and MEA

| Oxides (wt.%) | LHC | MEA | Minerals (wt.%) | LHC |
|---|---|---|---|---|
| CaO | 63.5 | 3.4 | $C_3S$ | 36.5 |
| $SiO_2$ | 20.9 | 4.3 | $C_2S$ | 44.3 |
| $Al_2O_3$ | 3.3 | 0.7 | $C_3A$ | 2.9 |
| MgO | 1.3 | 70.4 | $C_4AF$ | 13.3 |
| $Fe_2O_3$ | 4.9 | 1.0 | Anhydrite | 2.3 |
| $SO_3$ | 1.6 | 0.2 | | |
| Other oxides | 3.4 | 0.3 | | |
| Loss of ignition | 1.1 | 19.7 | | |

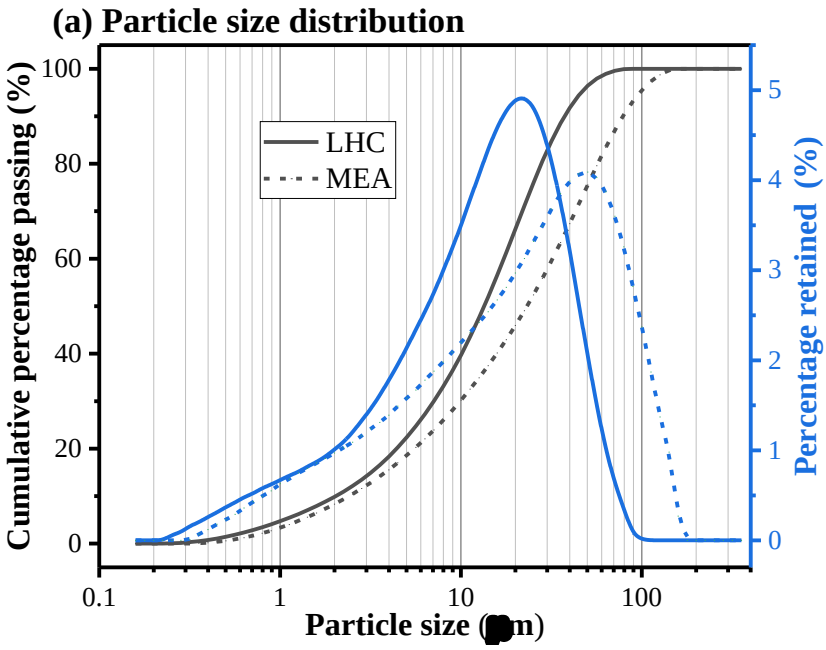
(a) Particle size distribution
Cumulative percentage passing (%)
Percentage retained (%)
LHC
MEA
Particle size (μm)
0.1
1
10
100
0
20
40
60
80
100
0
1
2
3
4
5

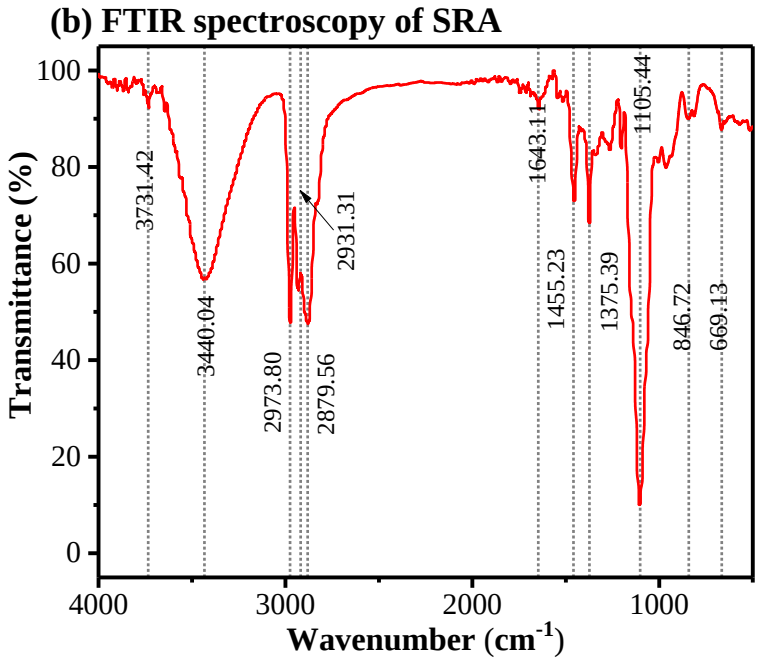
(b) FTIR spectroscopy of SRA
Transmittance (%)
Wavenumber (cm-1)
3731.42
3440.04
2973.80
2879.56
2931.31
1643.11
1455.23
1375.39
1105.44
846.72
669.13
4000
3000
2000
1000
0
20
40
60
80
100

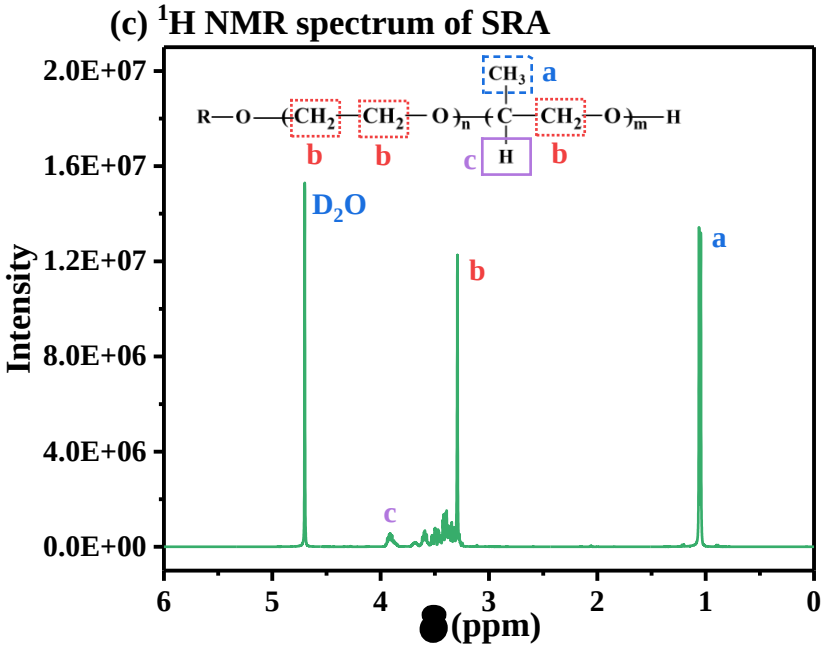


Fig. 1 Particle size distribution of LHC and MEA (a), FTIR spectroscopy of SRA (b), and $^1$H NMR spectrum of SRA (c)

### 2.2 Mix proportions

Based on the trial tests and works of literature [5][10][20], three variables and three levels shown in Table 2 were selected for the study. The levels of MEA and SRA were determined according to the suggested dosage and long-term shrinkage tests, while the levels of SP were set to make the paste flowable enough for rheological tests without bleeding. The water-to-binder ratio was kept constant at 0.35. The mix proportions used in this study are shown in Table 3. Taking M10S1.5P2 as an example, M10 stands for the dosage of MEA (10% by mass of LHC), and S1.5P2 means that the dosages of SRA and SP are 1.5% and 0.2% (by mass of powder materials), respectively. Here, No. 1-17 were designed based on the response surface methodology along with Box-Behnken Design on commercial software, Design-expert® 8.0.6. The interactions among MEA, SRA, and SP and their effects on dynamic rheological behaviour were then analysed.

### 2.3 Sample preparation

The weighted LHC and MEA were dry mixed first in the Hobart N50 mixer for 3 min. SP and SRA (if any) were then added to the deionized water and stirring for 1 min. When the possibly existing foams in the solution were eliminated, the mixing process started. The dry materials and water were mixed at a low speed of 140 rpm for 1 min and then stopped for 0.5 min to manually mix the paste with a spatula, followed by mixing at a high speed of 285 rpm for 2 min and another 1 min at low speed.

Table 2 Variables and levels applied in response surface design

| Levels | Variables | | |
|---|---|---|---|
| | MEA (%) | SRA (%) | SP (%) |
| -1 | 8 | 1.5 | 0.2 |
| 0 | 10 | 2.0 | 0.3 |
| 1 | 12 | 2.5 | 0.4 |

Table 3 Mix proportions of LHC pastes

| Sample | LHC (g) | Water (g) | MEA (g) | SRA (g) | SP (g) | Yield stress (Pa) | Plastic viscosity (Pa·s) |
|---|---|---|---|---|---|---|---|
| M10S1.5P2 | 450 | 167.5 | 50.0 | 7.5 | 1.0 | 13.870 | 0.963 |
| M12S2P2 | 440 | 165.0 | 60.0 | 10.0 | 1.0 | 15.784 | 1.189 |
| M12S2.5P3 | 440 | 162.5 | 60.0 | 12.5 | 1.5 | 13.729 | 1.113 |
| M12S2P4 | 440 | 165.0 | 60.0 | 10.0 | 2.0 | 5.372 | 0.880 |
| M10S2P3 | 450 | 165.0 | 50.0 | 10.0 | 1.5 | 11.936 | 0.859 |
| M12S1.5P3 | 440 | 167.5 | 60.0 | 7.5 | 1.5 | 11.299 | 0.897 |
| M10S2P3 | 450 | 165.0 | 50.0 | 10.0 | 1.5 | 7.908 | 0.943 |
| M10S2P3 | 450 | 165.0 | 50.0 | 10.0 | 1.5 | 9.260 | 0.779 |
| M10S2.5P2 | 450 | 162.5 | 50.0 | 12.5 | 1.0 | 12.512 | 0.909 |
| M8S2P2 | 460 | 165.0 | 40.0 | 10.0 | 1.0 | 11.283 | 0.974 |
| M10S1.5P4 | 450 | 167.5 | 50.0 | 7.5 | 2.0 | 2.494 | 0.725 |
| M8S1.5P3 | 460 | 167.5 | 40.0 | 7.5 | 1.5 | 2.391 | 0.601 |
| M10S2P3 | 450 | 165.0 | 50.0 | 10.0 | 1.5 | 9.950 | 0.824 |
| M10S2P3 | 450 | 165.0 | 50.0 | 10.0 | 1.5 | 10.265 | 0.893 |
| M8S2.5P3 | 460 | 162.5 | 40.0 | 12.5 | 1.5 | 5.726 | 0.877 |
| M8S2P4 | 460 | 165.0 | 40.0 | 10.0 | 2.0 | 0.372 | 0.524 |
| M10S2.5P4 | 450 | 162.5 | 50.0 | 12.5 | 2.0 | 0.799 | 0.643 |
| CS0P2 | 500 | 175.0 | / | / | 1.0 | / | / |
| CS2P2 | 500 | 165.0 | / | 10.0 | 1.0 | / | / |
| M10S0P2 | 450 | 175.0 | 50.0 | / | 1.0 | / | / |
| M10S2P2 | 450 | 165.0 | 50.0 | 10.0 | 1.0 | / | / |

## 2.4 Test methods

### 2.4.1 Rheological tests

The elapsed time is defined as the time after the initial contact of water and powder materials. At 7 min, the cement paste was transferred to the coaxial cylinder rotary rheometer (Atton Parr, Austria) for rheological tests, in which a concentric cylinder rotor with the diameter of 4 cm and the outer cylinder with the inner diameter of 4.194 cm were used. The temperature during the measurement was maintained at 25 °C by water bathing.

#### 2.4.1.1 *Dynamic shearing test*

To characterise the effects of MEA and SRA on the flowability of fresh cement paste after mixing, the dynamic shearing test was conducted, which was started at 10 min following the shear procedure: (1) increasing the shear rate linearly from 0 to 100 $s^{-1}$; (2) shearing for 30 s at the constant shear rate of 100 $s^{-1}$; and (3) decreasing the shear rate linearly from 100 $s^{-1}$ to 0. Every test was repeated three times independently to avoid the test error.

Bingham model as presented in Eq. (1) is one of the most commonly used rheological models for fitting the shear stress-shear rate curves [39]. In this paper, the Bingham model was selected to fit the down curve. According to the shear stress responses to the constant shear rate in Fig. 2, the shear stresses for each constant shear rates of 80 $s^{-1}$, 60 $s^{-1}$, 40 $s^{-1}$, and 20 $s^{-1}$ nearly remain constant. In those cases, the instant responses of shear stress are equal to the equilibrium-state values after shearing, each single shear stress is recorded in the steady state, thus, shear stress-shear rate curves in 80 $s^{-1}$ to 20 $s^{-1}$ of down curves are used for model fitting, the dynamic yield stress and plastic viscosity were obtained [39].

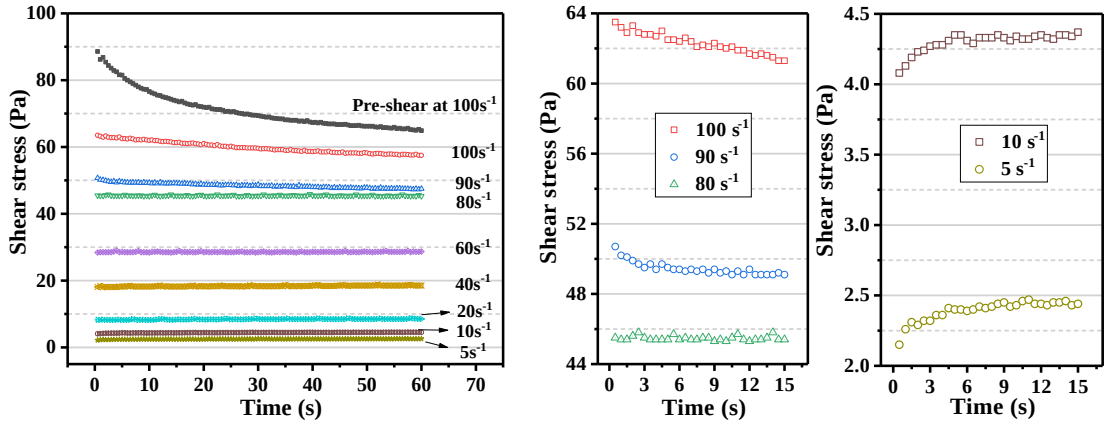


Fig. 2 Shear stress development of CS0P2 at constant shear rates

$$\tau = \tau_0 + \mu\dot{\gamma} \quad (1)$$

where $\tau_0$ is the dynamic yield stress (Pa), $\mu$ is the plastic viscosity (Pa·s), and $\dot{\gamma}$ is the shear rate.

2.4.1.2 *Static shearing test*

The static shearing test is commonly performed to measure the time-dependent rheological behaviour of cement paste. The contents of MEA and SRA were set as variables, while the SP content was fixed at 0.2% to avoid the disturbance of SP content on the results. LHC pastes with various dosages of MEA (0, 8%, 10%, 12%) and SRA (0, 2%) corresponding to samples M12S2P2, M8S2P2, CS0P2, CS2P2, M10S0P2, and M10S2P2 listed in Table 3 were selected for measuring the static yield stress. The test was started at 8.5 min, where the paste was first pre-sheared at 100 $s^{-1}$ for 0.5

min [40] and then stopped for 1 min to rebuild the structure of paste. A constant shear at 0.02 $s^{-1}$ was applied [41] at 10 min for 1 min and the data of 120 measure points were recorded. As a response to the constant shear, the shear stress increases gradually and reaches a peak value, followed by a decrease to a certain value, where the peak value was taken as the static yield stress [40]. The constant shear procedure was repeated every 10 min until the shear stress reached the maximum capacity of shearing stress (i.e. 450 Pa) or the elapsed time reached 120 min.

2.4.2 Isothermal calorimetry

Isothermal calorimetry was undertaken to investigate the effects of MEA and SRA on the early-age hydration process of LHC. The hydration heat of blends was measured on the TAM Air thermal activity micro-calorimeter. After mixing, about 12 g paste was weighed and transferred to the calorimeter. The test was started at 10 min after the contact of cement and water and the data were recorded every 30 s. The testing temperature was maintained at 25 °C.

2.4.3 Solid phase analyses

2.4.3.1 *Hydration stoppage*

At each specified age, i.e. 0.5, 1, 1.5, and 2 h, around 10 g paste was sampled and dispersed in 200 mL isopropanol and then stirred at 200 rpm in a beaker for 3 min to exchange the free water. Then the suspension was filtered and washed twice with isopropanol. These procedures were repeated twice to fully stop the hydration. Finally, the retained powder was washed with diethyl ether and then stored in a desiccator for 7 days before the microstructure tests and analyses on solid phase [42].

2.4.3.2 *Thermogravimetric analysis*

Main hydration products including CSH, AFt, $Mg(OH)_2$, and $Ca(OH)_2$ in this study were quantitatively analysed using TGA for their different decomposition temperatures, which was carried out with TGA 2(SF)-Mettler Toledo. The pre-processed dry powder samples were placed in an alumina crucible (70 μL) and the weight was controlled at around 50 mg. Then the powder samples were heated from 35 °C to 1050 °C at a rate of 10 °C/min under the $N_2$ atmosphere.

2.4.3.3 *X-ray diffraction*

The crystalline phases in hydrated blends were detected by X-ray diffraction tests. The dry powder sample was placed on a glass microscope slide and scanned at 25 °C on the Bruker D8 Advance diffractometer (CuKα radiation, 45mA, 35kV) at 6°/min in the range of 5~65°(2θ).

2.4.3.4 *Scanning electron microscopy*

The hydrate morphology of hydrated particles which is a dominant factor in the particle

interactions was observed using SEM. The dry powder sample was slightly sprayed on the conductive tape and then coated with platinum. The microscope (JSM-7900F) was used to take SEM images at an accelerating voltage of 15.0 kV.

2.4.3.5 *Specific surface area*

The porous hydration products covered on particles increase the surface roughness and contribute to the specific surface area. The nitrogen adsorption test (BET analysis) was conducted to determine the specific surface area of hydrated blends at 2 h, following a procedure recommended by Daake et al. [43] and Lou et al. [44].

2.4.4 Zeta potential test

Diluted suspensions with water-to-powder (W/P) ratio of 10 and 50 were prepared for zeta potential tests [42] that were conducted on ZetaProbe (Colloidal Dynamics. Inc, America) in two approaches. For the first approach, the W/P ratio is 10, which is used for the instant measurement realating to the dynamic shearing test. The powder materials and chemical admixtures were mixed with deionized water. After stirring at 300 rpm for 3 min, the suspension was transferred to the measuring cell. The tests were then carried out to explore the combined effect of SP and SRA. For the second approach, the W/P ratio is 50, which is related to the time-dependent rheological properties. We followed the mixing and hydration stoppage procedures and obtained dry powder samples at ages of 0.5, 1, 1.5, and 2 h, which were re-dispersed in the deionized water. In this way, the diluted suspensions at specified hydration time and solid mass fraction were prepared. Then, the suspensions were transferred to the measuring cell to obtain the zeta potential at each hydration age. During the measurement, the suspension was stirred at 250 rpm to keep it homogeneous. The zeta potential was measured by the electrodes in the measuring cell and then calculated using the embedded software based on the O'Brien equation [45].

## 3 Results and discussion

### 3.1 Dynamic rheological parameters

The dynamic yield stress and plastic viscosity of fresh blended pastes (see in Table 3) were obtained by fitting the shear stress-shear rate curves with the Bingham model. The individual effects of MEA, SRA, and SP on the dynamic rheological parameters were illustrated by single-factor analyses. Afterwards, the analyses based on response surface methodology were conducted on the dynamic yield stress and plastic viscosity.

3.1.1 Single-factor analyses

Based on the variables and levels listed in Table 2, the single-factor analyses of the dynamic yield stress and plastic viscosity were conducted. It is worth mentioning that the SP dosage was fixed at 0.2% for the single-factor test on MEA and SRA to ensure the paste is flowable enough for the dynamic shearing test. The effects of the individual use of SP, MEA, and SRA in LHC pastes are shown in Fig. 3. The results show that the addition of SP favours the flowability of LHC paste, where both dynamic yield stress and plastic viscosity decrease significantly with the dosage of SP. The effect of MEA on dynamic yield stress and plastic viscosity is consistent with the review in the introduction part that MEA aggravates the flocculation and increases the water demand, thus leading to the increase of dynamic yield stress and plastic viscosity. In comparison with the other two factors, it is apparent that SRA exhibits a more complicated effect. At the given dosage range of SRA (1.5%-2.5%), the extremum values are observed at an intermediate dosage, i.e. the minimum of dynamic yield stress and the maximum of plastic viscosity. With the increase of SRA dosage, the dynamic yield stress decreases first and then increases, whereas the plastic viscosity increases first and then decreases.

From the single-factor analyses as presented in Fig. 3, a declined trend with SP and a rising trend with MEA on both dynamic yield stress and plastic viscosity are obtained. But the role of SRA is dependent on its dosage for its nature as the water-soluble polymer, the adsorption of SRA molecules, and steric hindrance effect, as well as the lubrication effect all contribute to the dynamic rheological behaviours. A similar controversy on the effect of SRA on workability has also been reported in literature [33, 34]. Based on the single-factor analyses and measured results listed in Table 3, the dynamic yield stress and the plastic viscosity with the combined use of MEA, SRA, and SP were further analysed by response surface methodology.

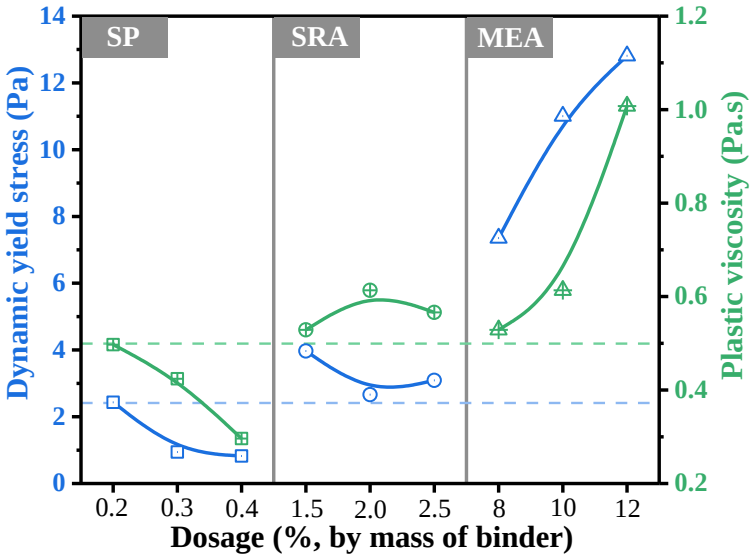

Fig. 3 Effects of SP, SRA, and MEA on dynamic yield stress and plastic viscosity of LHC paste

3.1.2 Dynamic yield stress

The response surface methodology including three variables and three levels is used to fit experimental data with a quadratic regression equation, the interactions between factors on the dependent variable can be obtained. The variables A, B, and C represent MEA, SRA, and SP, respectively. The regression model on dynamic yield stress is shown in Eq. (2). The variance analysis (ANOVA) of the dynamic yield stress is presented in Table 4, where $R^2_{Adj}$ is a modification value of $R^2$ by parameters in the model. $R^2_{Adj}$=0.8438 implies that this model fits the actual data well. The relationship between the predicted values and the actual ones is shown in Fig. 4a. The value of the correlation coefficient ($R^2$) of the model is 0.9317, which suggests that this model well fits the experimental data. As shown in Table 4, the P-value of the regression model means whether it is statistically significant. The P-value of Lack of Fit is 0.1878, which is higher than the limit value of 0.05, indicating that the Lack of Fit is not significant in the model. Among the factors acting on the dynamic yield stress, MEA and SP are predominant factors (P<0.01), while SRA is not a statistically significant factor (P-value>0.05). In summary, the results of $R^2$, $R^2_{Adj}$, P-value of Lack of Fit all show that the regression model is statistically significant. The contribution ratios of three factors on dynamic yield stress, obtained from the F-test and P-value, indicate that C>A>B, i.e. SP>MEA>SRA. As reflected in Fig. 4b-g, effects of variables and levels can be drawn.

$$\tau_0 = -35.191 + 3.899A + 22.339B + 1.745C - 0.226AB + 0.062AC - 0.168BC - 0.099A^2 - 4.723B^2 - 1.264C^2 \quad (2)$$

Table 4 Analysis of variance for the dynamic yield stress

| Source | Sum of squares | Degree of freedom | Mean square | F-value | P-value | |
|---|---|---|---|---|---|---|
| Model | 349.4639 | 9 | 38.82933 | 10.60454 | 0.0026 | significant |
| A | 87.19674 | 1 | 87.19674 | 23.814 | 0.0018 | |
| B | 0.920284 | 1 | 0.920284 | 0.251335 | 0.6315 | |
| C | 246.5544 | 1 | 246.5544 | 67.3356 | < 0.0001 | |
| AB | 0.204822 | 1 | 0.204822 | 0.055938 | 0.8198 | |
| AC | 0.062313 | 1 | 0.062313 | 0.017018 | 0.8999 | |
| BC | 0.028314 | 1 | 0.028314 | 0.007733 | 0.9324 | |
| $A^2$ | 0.662029 | 1 | 0.662029 | 0.180804 | 0.6834 | |
| $B^2$ | 5.8706 | 1 | 5.8706 | 1.603299 | 0.2459 | |
| $C^2$ | 6.72783 | 1 | 6.72783 | 1.837414 | 0.2174 | |
| Residual | 25.63103 | 7 | 3.661575 | | | |
| Lack of Fit | 16.97889 | 3 | 5.659628 | 2.616521 | 0.1878 | not significant |
| Pure Error | 8.652143 | 4 | 2.163036 | | | |

| | | |
|---|---|---|
| Cor Total | 375.095 | 16 |
| $R^2$=0.9317, $R^2_{Adj}$=0.8438 | | |

The contour shape and the slope of the response surface, as presented in Fig. 4, reflect the significance of the interactions of any two factors among MEA, SRA, and SP. Fig. 4b and c show the interaction of SRA and MEA on the dynamic yield stress. The dosage of SRA exerts less influence and is less significant than that of MEA on the dynamic yield stress. When the dosage of MEA is fixed in the range of 8-10%, the dynamic yield stress increases first and then decreases with the increasing SRA dosage, which is contradictory with the result from single-factor analysis on the neat LHC paste.

Fig. 4d and e present the interaction of SP-MEA, which is the most significant one in the model. When the content of MEA increases in the range of 8-12%, the dynamic yield stress greatly increases. While the opposite trend is observed with the increasing SP dosage. When the contents of SP and MEA are kept at a certain proportion, the dynamic yield stress holds steady (e.g. the blend with 10% MEA and 0.3% SP has nearly equal dynamic yield stress with the blend with 12% MEA and 0.4% SP).

Fig. 4f and g show the moderate interaction between SP and SRA. The effect of SP on the dynamic yield stress is influenced by the SRA dosage. Namely, when the SP dosage is fixed in the range of 0.2-0.4%, the dynamic yield stress increases first and then decreases with the increasing SRA dosage. In other words, the effect of SRA is also altered by SP due to the potential interactions between polymers. The result is also contradictory with the effect of SRA on LHC paste from the single-factor analysis.

(a) Relation between predicted and actual values

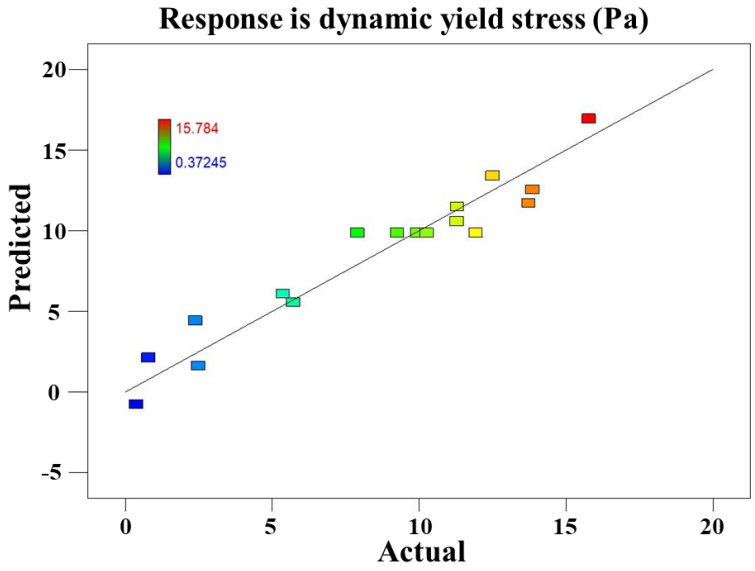


(b) Contour of AB

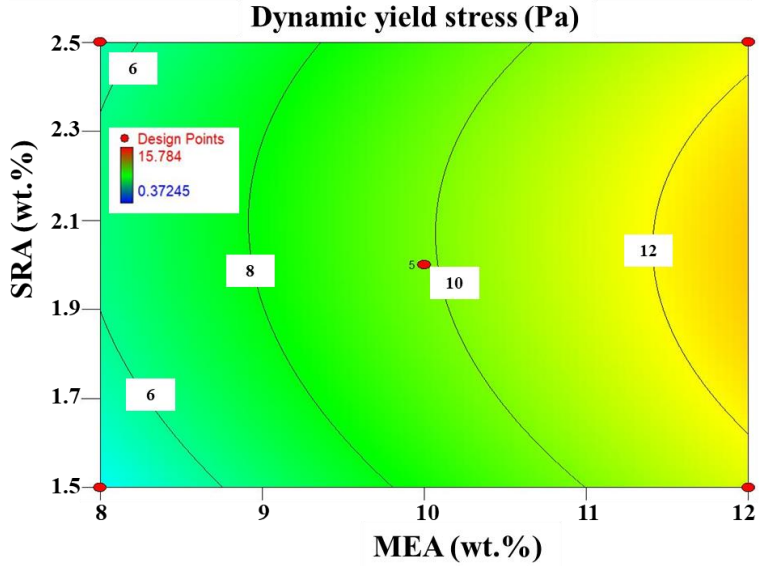


(c) Response surface of AB

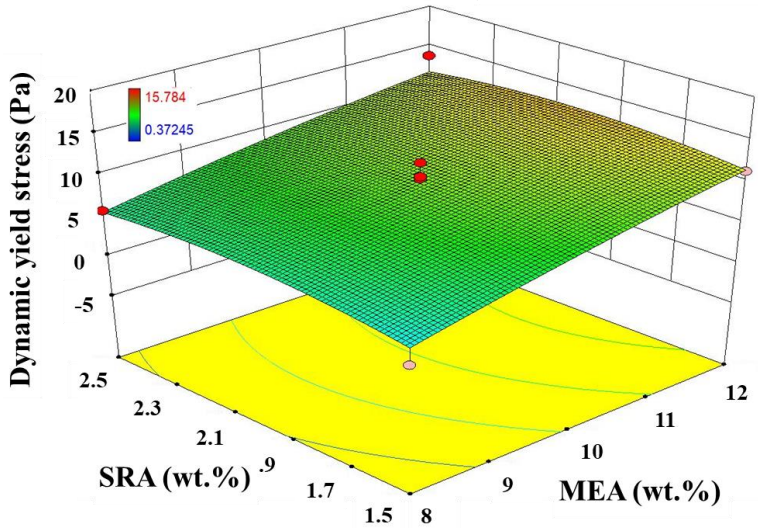

(d) Contour of AC

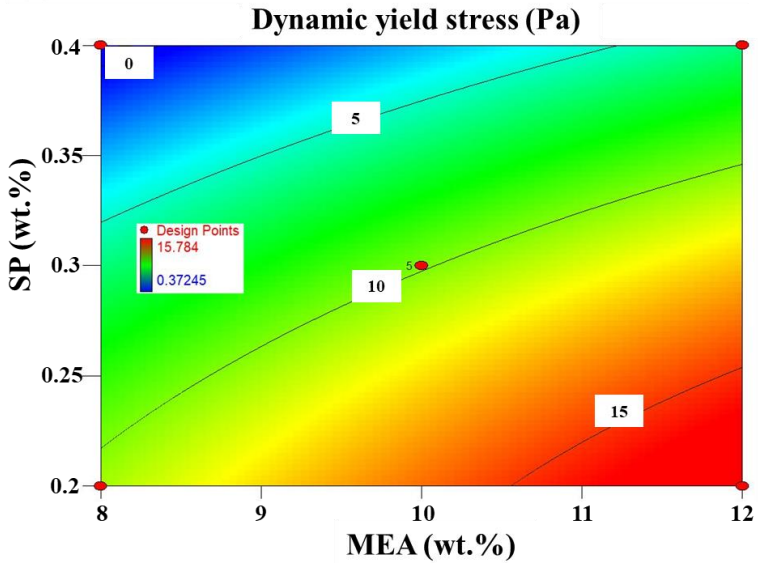


(e) Response surface of AC

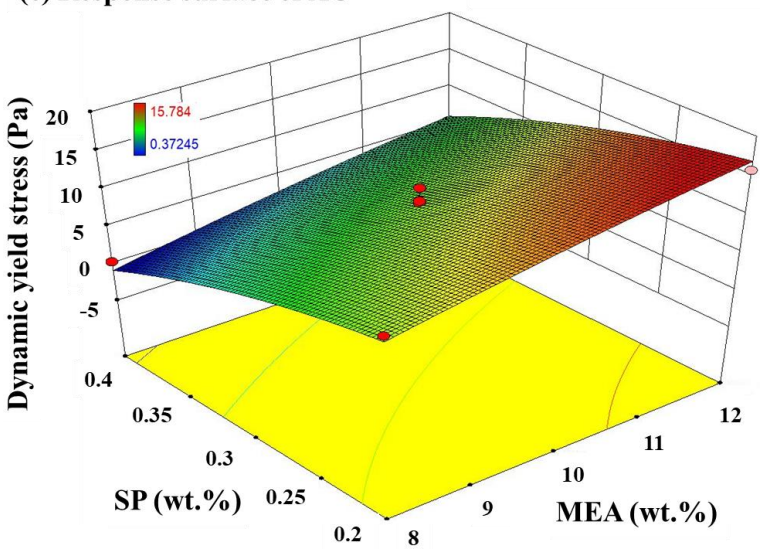


(f) Contour of BC

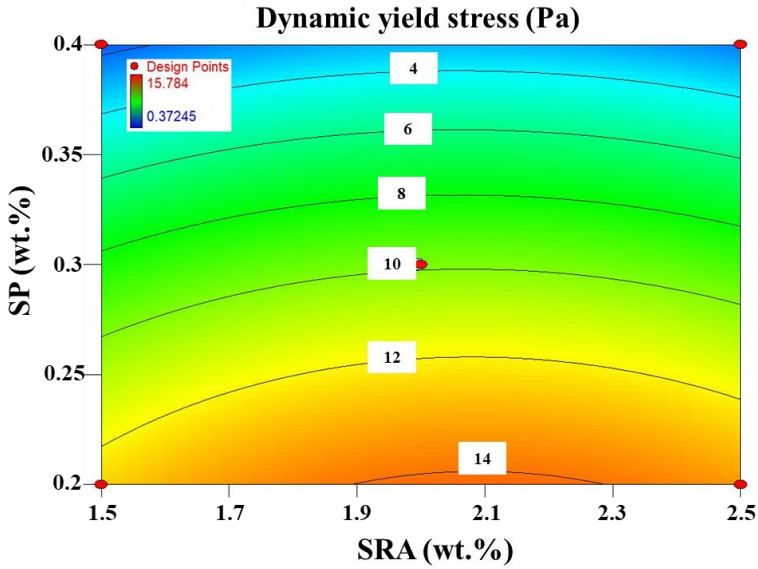

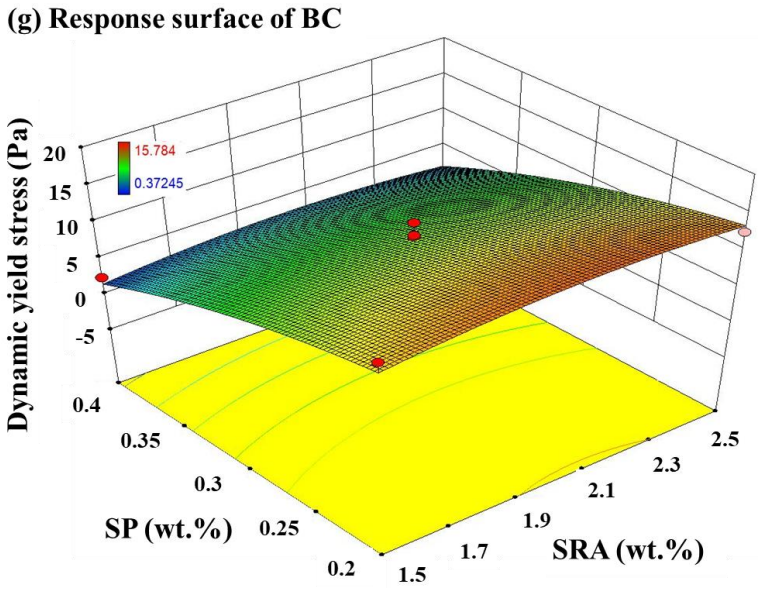


Fig. 4 Data obtained from the regression model of the dynamic yield stress

3.1.3 Plastic viscosity

The regression model of the plastic viscosity is shown in Eq. (3). The variables A, B and, C stand for MEA, SRA, and SP respectively. Table 5 presents the variance analysis (ANOVA) of plastic viscosity. Among three factors acting on the plastic viscosity, MEA and SP are predominant factors ($P<0.01$), SRA is not a statistically significant factor. The relationship between the predicted values and the actual ones is shown in Fig. 5a. The data shown in Table 5 and Fig. 5a indicate that the model is statistically significant and can fit the experimental data. But the correlation between predicted values and the actual plastic viscosity is poorer than the former model. Moreover, $R^2_{Adj}=0.6364$ means that the goodness of fit of this model is also poorer. The reason can be attributed to that the measured pastes are highly flowable and some fitted plastic viscosity values are close to each other, thereby affecting the model sensitivity with variables. Based on results from F-test, the contribution ratios of three factors on plastic viscosity are as follows: C>A>B, i.e. SP>MEA>SRA. As reflected in Figs. 5b-g, effects of variables and levels on the plastic viscosity can be drawn.

$$\mu = 1.107 - 0.191A + 0.836B - 0.218C - 0.015AB + 0.018AC - 0.014BC + 0.012A^2 - 0.139B^2 - 0.015C^2 \quad (3)$$

Table 5 Analysis of variance for the plastic viscosity

| Source | Sum of squares | Degree of freedom | Mean square | F-value | P-value | |
|---|---|---|---|---|---|---|
| Model | 0.388668 | 9 | 0.043185 | 4.11185 | 0.0378 | significant |
| A | 0.152449 | 1 | 0.152449 | 14.51525 | 0.0066 | |
| B | 0.015811 | 1 | 0.015811 | 1.505438 | 0.2595 | |

| | | | | | | |
|---|---|---|---|---|---|---|
| C | 0.199676 | 1 | 0.199676 | 19.01201 | 0.0033 | |
| AB | 0.000886 | 1 | 0.000886 | 0.084355 | 0.7799 | |
| AC | 0.004966 | 1 | 0.004966 | 0.472835 | 0.5138 | |
| BC | 0.000186 | 1 | 0.000186 | 0.017744 | 0.8978 | |
| $A^2$ | 0.009432 | 1 | 0.009432 | 0.898033 | 0.3749 | |
| $B^2$ | 0.005113 | 1 | 0.005113 | 0.486809 | 0.5079 | |
| $C^2$ | 0.000921 | 1 | 0.000921 | 0.087684 | 0.7757 | |
| Residual | 0.073519 | 7 | 0.010503 | | | |
| Lack of Fit | 0.057688 | 3 | 0.019229 | 4.858654 | 0.0804 | not significant |
| Pure Error | 0.015831 | 4 | 0.003958 | | | |
| Cor Total | 0.462186 | 16 | | | | |
| $R^2$=0.8409, $R^2_{Adj}$ =0.6364 | | | | | | |

Fig. 5 presents the significance of the interactions among three factors on the plastic viscosity. Fig. 5b and c show the effect of SRA on the plastic viscosity in presence of MEA. With a high dosage of MEA in the range of 10-12%, the plastic viscosity increases first and then slightly decreases with SRA dosage, which is consistent with the single-factor analysis. With a low dosage of MEA in the range of 8-10%, the plastic viscosity increases more sharply with the increasing SRA dosage.

Similarly, the interaction between SP and MEA also shows the highest significance, as seen in Fig. 5d and e, the plastic viscosity increases with the increasing content of MEA but decreases with SP addition. In Fig. 5f and g, when the SP dosage is kept constant, the plastic viscosity growth first increases with the increasing SRA content and then slightly decreases, which is also consistent with the single-factor analysis.

The interactions between MEA, SRA, and SP affected the dynamic rheological properties and were resolved by response surface analyses. Concerning LHC pastes with MEA addition, MEA enlarges the water demand of the powder materials, thereby increasing the dynamic yield stress and plastic viscosity. In both fresh and hardened cement-based materials, the mechanisms of SP and SRA are summarized as adsorptions of molecules on air-liquid and liquid-solid interfaces [46]. It is apparent from the single-factor analyses (see Fig. 3) that SRA decreases first then increases the dynamic yield stress of neat LHC paste, however, an opposite trend on the plastic viscosity is observed. But the interactions of MEA-SRA and SP-SRA, as seen in Fig. 4 and 5, show different roles of SRA in LHC paste with MEA in comparison with the single-factor analyses on neat LHC paste. The dynamic yield stress and plastic viscosity both increase first then decrease with SRA dosage. Based on those experimental findings above, the principle on designing the initial flowability of LHC paste with MEA, SP, and SRA can be drawn.

However, the use of MEA seems to change the effect of SRA on the dynamic yield stress in presence of SP, the mechanism is still unclear. In Fig. 5b, we find that the plastic viscosity increases with SRA dosage at relatively low MEA content; But the plastic viscosity barely changes at relatively high MEA content. Therefore, the zeta potential values of LHC paste and fresh blends of LHC and MEA were measured to further revealing the interaction of SP and SRA.

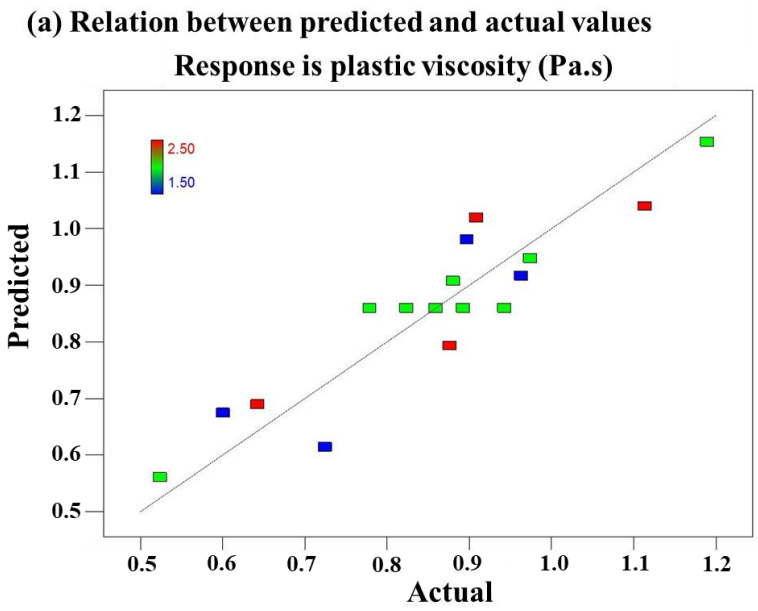


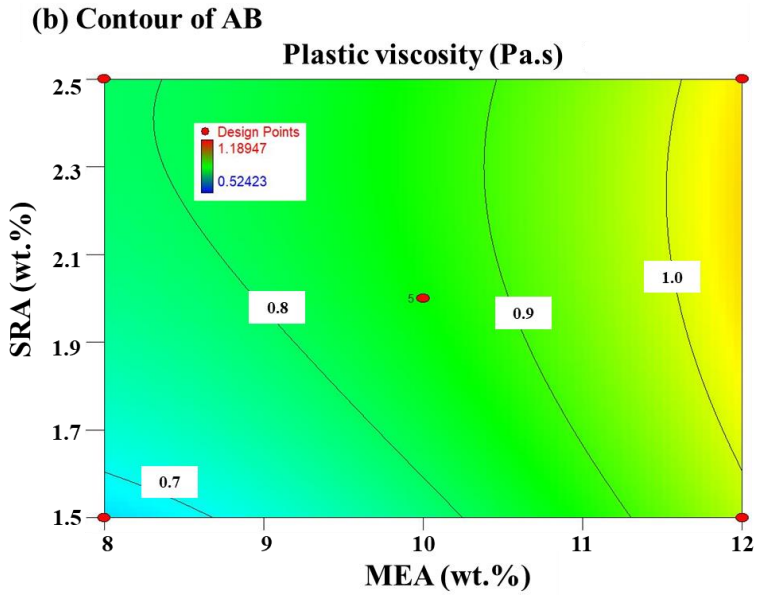

(c) Response surface of AB

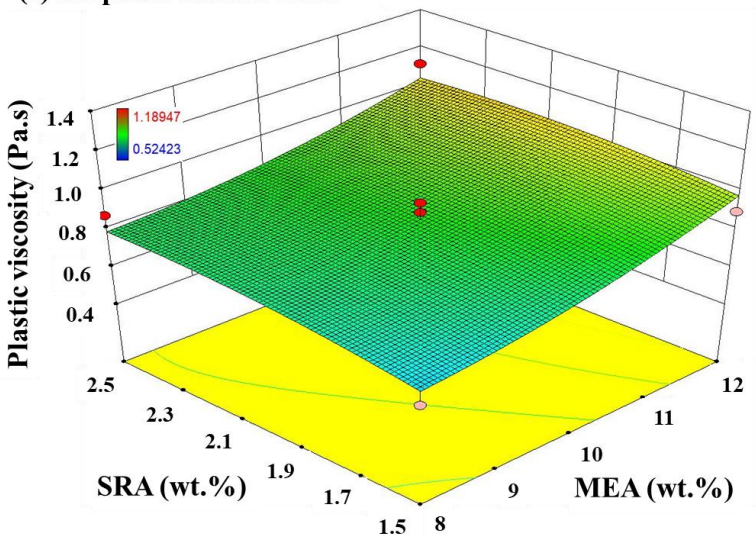


(d) Contour of AC

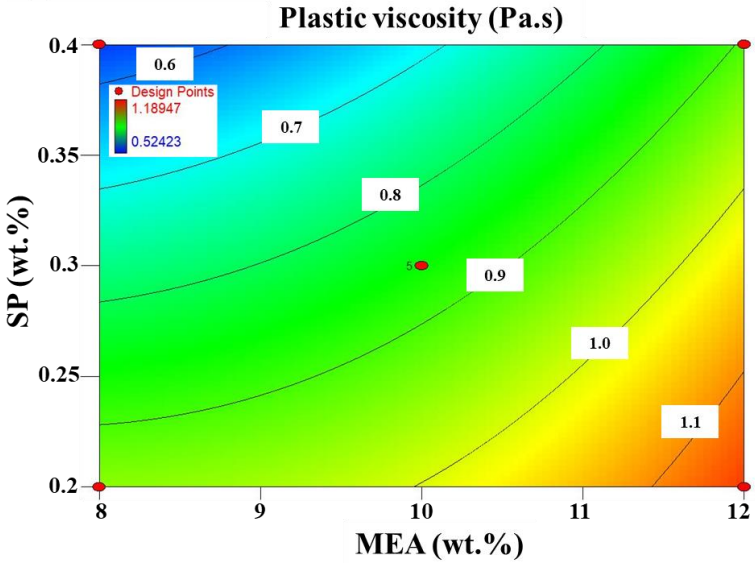


(e) Response surface of AC

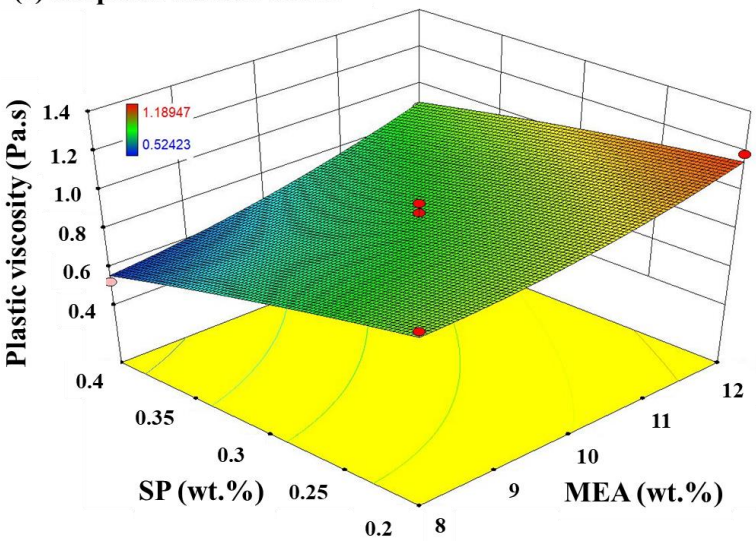

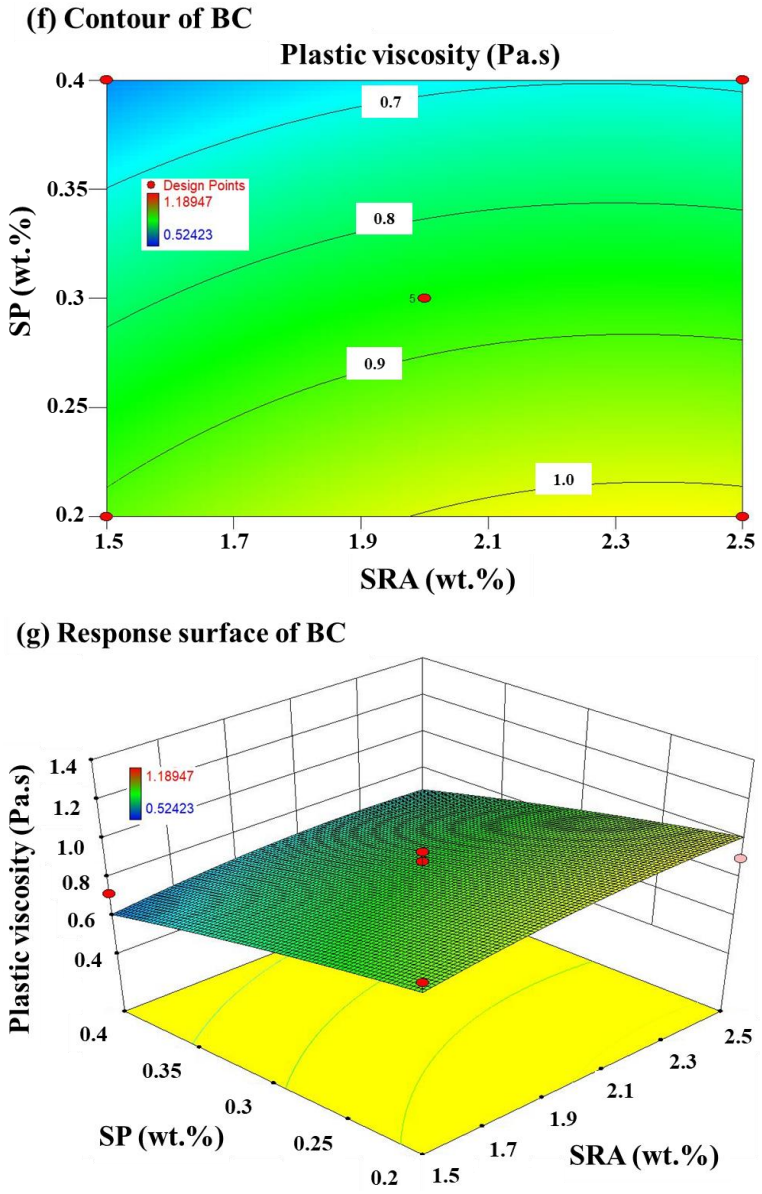


Fig. 5 Data obtained from the regression model of the plastic viscosity

3.1.4 Roles of SP and SRA

Fig. 6 shows the effects of SRA and SP on the zeta potential of two suspensions, i.e. neat LHC and blend of 90% LHC and 10% MEA, with a W/P ratio of 10. As seen in Fig. 6a, the zeta potential values of the two suspensions are all positive. The zeta potential values of the latter suspension are significantly higher, because the surface charge of MgO grain is much higher than that of the cement grains [30], thereby resulting in a higher zeta potential value of LHC-MEA suspension than that of LHC suspension.

In Fig. 6 there is a clear trend that the zeta potential value gradually decreases with the increasing dosage of SP, while it basically remains unchanged with SRA addition. To evaluate the possible competitive adsorption between SP and SRA molecules on the particle surface in suspensions, different adding sequences of SP and SRA were adopted for the sample preparation for zeta potential

tests. Three adding sequences listed in Fig. 6b are as follows: (1)-SP and SRA were premixed in water before preparing the suspension; (2)-Only SRA was premixed in water to prepare the suspension, SP was added to the well-mixed suspension, and stirred for another 2 min; (3)-Only SP was premixed in water to prepare the suspension, no SRA was used.

As shown in Fig. 6b, no significant difference is found on the zeta potential with the first two adding sequences of SP. The premixed SP and SRA, i.e. adding sequence (1), only slightly increases the zeta potential at high SP dosages (0.3% and 0.4%) than that of the subsequent addition of SP, i.e. adding sequence (2). Plank et al. [16] reported the competitive adsorption of SP and retarder molecules in cement suspension. The adsorptions of SP or retarder both lead to a notable variation trend of zeta potential by changing the surface charge density. In this paper, the highest dosage of SRA is 2.5% by mass of binder, which is much higher than that of SP and can reach the amount of saturation adsorption. However, as shown in Fig. 6a, no significant difference in the zeta potential is observed with the increasing SRA dosage, it can be expected that the SRA molecule is not adsorbable or the adsorbed SRA does not change the surface charge of particles in above suspensions. Nevertheless, results presented in Fig. 6b show that the combined use of SRA and SP results in higher zeta potential values in comparison with the individual use of SP. The result confirms the adsorption of SRA on the particle surface or on the SP molecule, which can change the zeta potential of suspensions with SP. Therefore, no evident competitive adsorption between SP and SRA is observed from zeta potential results as presented in Fig. 6b.

Generally, high absolute values of the zeta potential contribute to a repulsive force and dispersion of particles in suspension, thereby improving the flowability of paste. In the above suspensions, SP decreases the absolute values of zeta potential with the increasing dosage. It is attributed to the adsorption of charged SP molecules on the particle surface [16], then the steric hindrance effect of SP notably increases the flowability. The roles of SP and SRA molecules in blends can be concluded as adsorbing on particle surface, changing the surface-to-surface separation distance, and interstitial fluid viscosity [29]. Due to the effect of preferential adsorption, the larger molecules (i.e. the comb-type polymer of SP in this paper) tend to adsorb on the cement grain surface, while the smaller molecules (i.e. the linear polymer of SRA in this paper) are left in the pore solution. Moreover, Fig. 6b shows that SRA may also adsorb on the SP molecules that are adsorbed on the cement grains [47], thereby resulting to a different result of adding sequence (1) from the other two. Then the combined effect of SRA and SP can be explained by roles of “adsorbing polymer” and “nonadsorbing polymer”

as described in [29][47]. At low SRA dosage, SRA molecules partially adsorb and partially disperse in the pore solution, the adsorbed SRA molecules leads to lower zeta potential values, while nonadsorbing SRA molecules contributes to the depletion flocculation of particles [47], thereby increasing the yield stress and viscosity. At high dosage, nonadsorbing SRA molecules increase with the SRA dosage and decrease the interstitial fluid viscosity at the constant solid volume fraction, which slightly reduces the friction in the suspension and favours the flowability. However, the average surface-to-surface separation distance also changes with the polymer dosage and is a function of the initial solid volume fraction, thus, this is the reason that addition of MEA changes the effect of SRA on dynamic parameters in neat LHC paste.

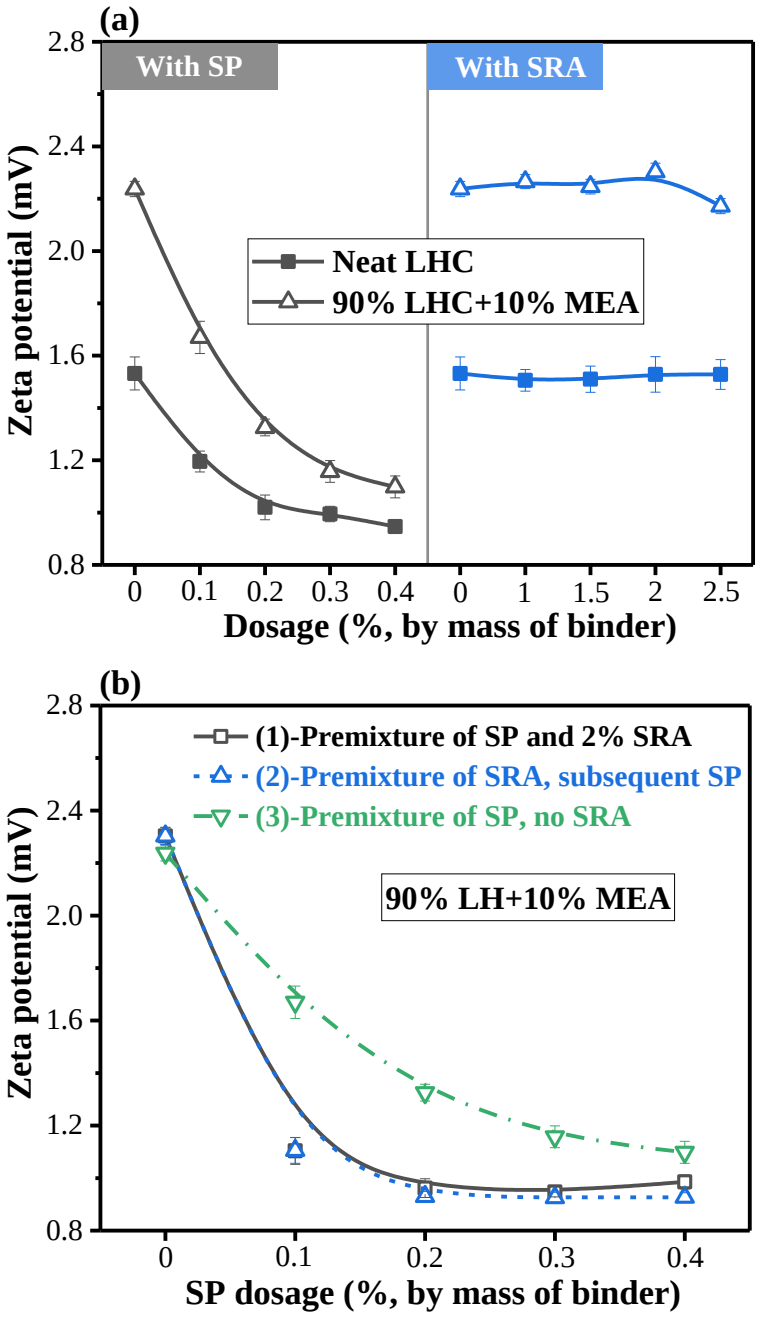


Fig. 6 Zeta potential of suspensions with W/P ratio of 10

### 3.2 Static rheological parameters

#### 3.2.1 Evolution of static yield stress

The evolution of static yield stress is usually related to the structural build-up of cement paste [40, 41, 48], which is considered as the key parameter for 3D printing [49, 50], formwork pressure [51], and distinct layer casting [52] of cement-based materials. The evolution of static yield stress with the elapsed time of blends is shown in Fig. 7. The parameters are further summarized in Table 4, where the growth rate is denoted as the slope in 20-120 min. With the increase of SRA from 0 to 2%, the growth rate increases by 1.15 times as well as the peak value by 1.04 times of the static yield stress of the LHC paste. As mentioned above, the addition of 10% MEA decreases the flowability and increases the dynamic yield stress of pastes, as a result, the initial static yield stress (at 10 min) also increases. With regard to the static yield stress development as shown in Table 4, the peak value and growth rate of the LHC paste are increased by 1.68 times and 1.56 times respectively with 10% MEA. Moreover, a positive correlation between the growth rate of static yield stress and MEA content is observed. As shown in Table 1, the main component of MEA, MgO, reacts with water in an alkaline solution to form brucite, i.e. $Mg(OH)_2$. The brucite crystals grow on the surface of MgO particles and increase the surface roughness. With the hydration going on, the particle interactions as well as the bridging effect of brucite crystals and other hydrates contribute to the more rapid development of static yield stress.

Interestingly, a comparison of M10S0P2 and M10S2P2 reveals that SRA is more effective in accelerating the static yield stress growth in blends of LHC and MEA than that of LHC paste, of which the nominal values are 2.33/1.68 vs. 1.15/1.00 respectively. As mentioned above, with the increasing dosage of SRA, the dynamic yield stress increases first and then decreases in LHC-MEA blends. However, an opposite trend with the increasing SRA dosage was observed in neat LHC paste. By contrast, adding 2% SRA significantly increases the growth rate of the static yield stress of pure LHC paste and blends of LHC and MEA. The physical definitions of the dynamic yield stress and static yield stress are similar, which correspond to the stress that the paste starts to flow, but the test procedures are quite different [39]. As shown in Figs. 3 and 4, the effect of SRA on the dynamic yield stress is mainly involved in the physical interaction of SRA molecules and the cement suspension, it cannot account for the increasing growth rate of the static yield stress which is a complex physicochemical process. The reason may be those hydration products in LHC and blends of LHC and MEA are all affected by SRA [6, 30, 31], while the reaction of MEA is also affected at the early

age, the mechanisms will be discussed later.

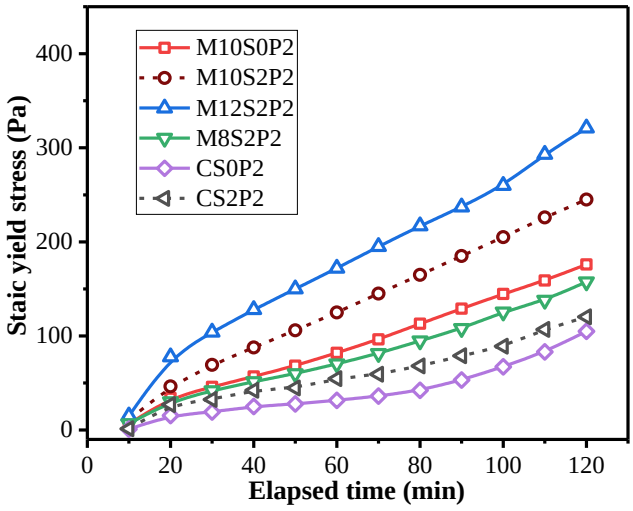


Fig. 7 Evolution of static yield stress of blends

Table 4 Parameters of blended pastes by static shearing tests

| Mix | Peak value (Pa) | | Growth rate (Pa/min) | |
|---|---|---|---|---|
| | Measured value | Nominal value | Measured value | Nominal value |
| CS0P2 | 105.0 | 1.00 | 0.90 | 1.00 |
| CS2P2 | 120.3 | 1.15 | 0.93 | 1.04 |
| M10S0P2 | 176.0 | 1.68 | 1.42 | 1.58 |
| M10S2P2 | 245.0 | 2.33 | 1.99 | 2.22 |
| M8S2P2 | 157.5 | 1.50 | 1.27 | 1.42 |
| M12S2P2 | 321.0 | 3.06 | 2.43 | 2.72 |

### 3.2.2 Hydration and solid phase assemblage

The calorimetric results are shown in Fig. 8, in which the dosage of SP is fixed at 0.2%, the single or combined effects of MEA and SRA are detected on the hydration of LHC with SP. With 10% MEA addition, the induction period is shortened and the initial cumulative heat increases, and time to reach the main peak and the peak value of the heat release rate are reduced. As a comparison, SRA retards the hydration process of LHC and leads to lower initial heat and more gradual acceleration, the main exothermic peak is delayed and the cumulative heat decreases. In comparison with CS2P2, the induction period of M10S2P2 is shortened, and the main exothermic peak appears earlier.

In summary, MEA accelerates the hydration of LHC but the accelerating effect is weakened at the later age on the cumulative heat, while SRA shows a notable retarding effect during the test period. When MEA and SRA are used simultaneously, their effects are time-dependent. In the first 4 h, the reaction of MgO promotes the heat release and shortens the induction period. During the period of 4-

16 h, the retarding effect of SRA appears, thus affecting the exothermic peak and reducing the cumulative heat. During the period of 16-24 h, SRA shows the negligible effect on the exothermic rate, exothermic rates of LHC pastes are even higher than that of LHC and MEA blends, and their cumulative heat approaches gradually.

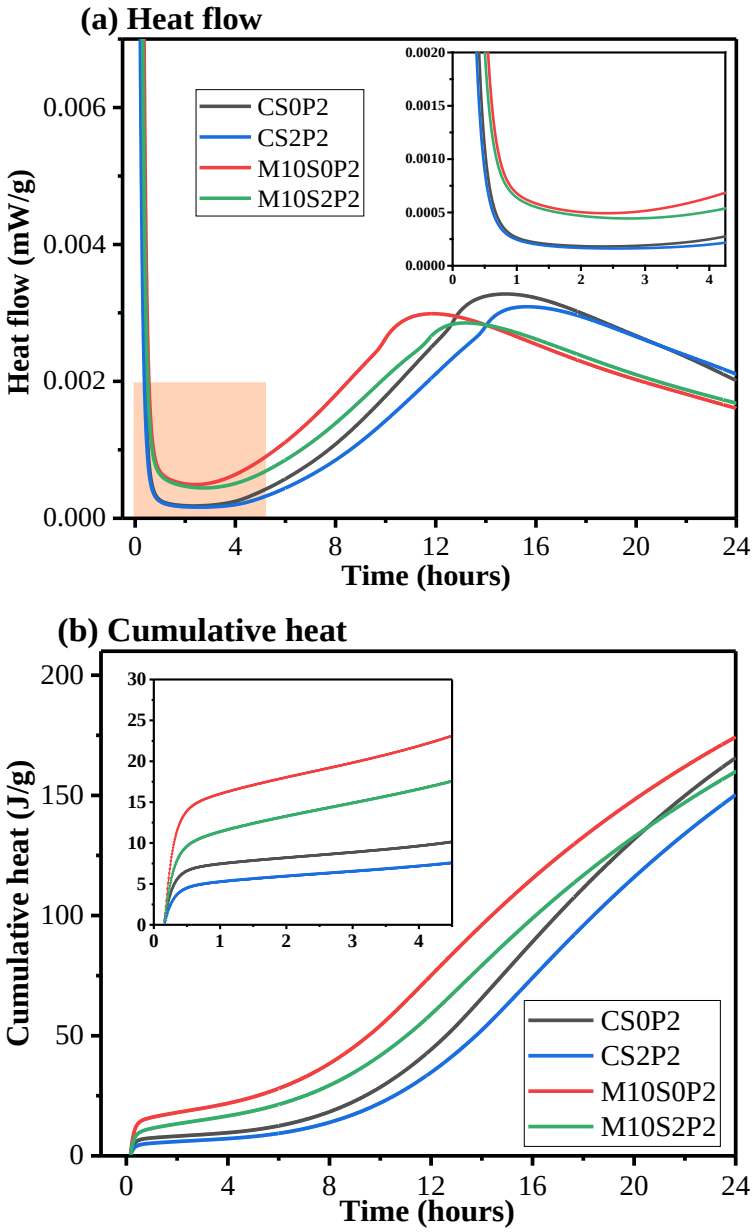


Fig. 8 Hydration heat of blends composed of LHC, MEA, and SRA with SP

To assess the solid phase compositions of blends, XRD, and TGA were conducted on hydrated blends. To identify the hydration products, XRD tests were carried out first. Fig. 9 shows the XRD patterns of unhydrated LHC, hydrated blends with and without SRA. As shown in the figure, the main diffraction peaks are unhydrated clinkers and periclase, i.e. MgO. The reaction product of MEA, i.e. brucite, is not clearly observed. Moreover, the main hydrates of cement, as well as the effect of SRA are also not observed from the patterns. León-Reina [53] reported that the precision of the Rietveld

analysis varies from 0.6-1.2 wt.% for some crystalline phases of cement hydration products. In this study, only a small amount of clinkers is consumed in the first 2h, so the same for the formation of brucite and other hydrates of LHC. Therefore, it's difficult to directly determine the formation amount of cement hydrates and $Mg(OH)_2$ by Quantitative XRD at a very early age. As a complementary technique, TGA was used to quantitatively measure the contents of $Ca(OH)_2$ and $Mg(OH)_2$ at 0-2 h.

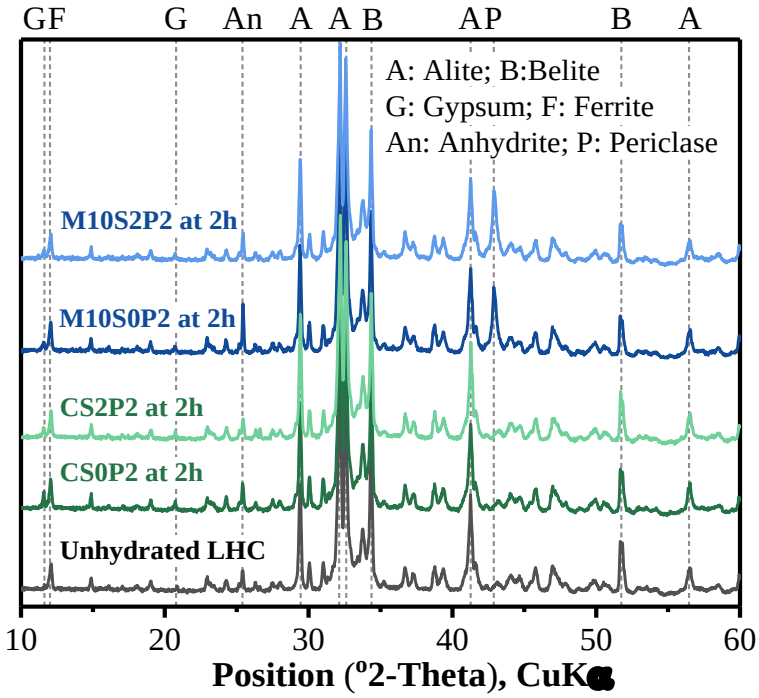


Fig. 9 The XRD patterns of blends composed of LHC, MEA, and SRA with SP (A=Alite, B=Blite, F=Ferrite, P=Periclase, G=Gypsum, An=Anhydrite)

Fig. 10 shows the TGA results of blends with and without SRA cured for different ages. As seen in Fig. 10a to d, there are 3 main decomposition peaks in LHC blends, and 4 peaks in blends of LHC and MEA. CSH and/or ettringite decompose at around 90 °C, the weight loss between 120-170 °C is attributed to the decomposition of gypsum. The peaks around 340 °C and around 420 °C stems from the decomposition of brucite and portlandite, respectively.

Generally, structural build-up, i.e. evolution of static yield stress in this paper, is considered as closely relating to the hydrate amount of cement, mainly C-S-H [35, 54] and ettringite [42]. However, it is difficult to quantitatively analyse the solid phase change of Portland cement at a very early age. The contents of $Ca(OH)_2$ and $Mg(OH)_2$ in this paper were used to reflect the reaction degree of LHC and MEA, respectively. As shown in Fig. 10a and b, adding 2% SRA retards the hydration process of LHC. The portlandite content in the first 2 hours is reduced due to the retarding effect of SRA, but the static yield stress notably increases during this period. Similarly, the results presented in Fig. 10c and d show that the contents of $Mg(OH)_2$ are also affected by SRA at 0.5-2h. The contents of $Ca(OH)_2$

and $Mg(OH)_2$ are further summarized in Fig. 10e. As seen in Fig. 10e, adding MEA leads to more $Ca(OH)_2$ formation, which confirms the acceleration effect of MEA on LHC hydration. In the previous section, the acceleration effect on the static yield stress growth by MEA is attributed to the hydration product, $Mg(OH)_2$. It's worth noting that the content of $Mg(OH)_2$ from Fig. 10e is around three times of $Ca(OH)_2$ in M10S0P2 and M10S2P2. The formation of $Mg(OH)_2$ seems to play an important role in promoting the growth of static yield stress in fresh blended pastes.

Fig. 10e also presents that 2% SRA significantly reduces the amount of $Mg(OH)_2$ as detected by TGA. Moreover, $Ca(OH)_2$ contents in the neat LHC paste and blends of LHC and MEA are all reduced by SRA. With less amount of reaction products, why do M10S2P2 exert an even much higher growth rate of the static yield stress? To answer this question, the zeta potential of re-dispersed suspensions, BET analysis, and SEM observations were further conducted.

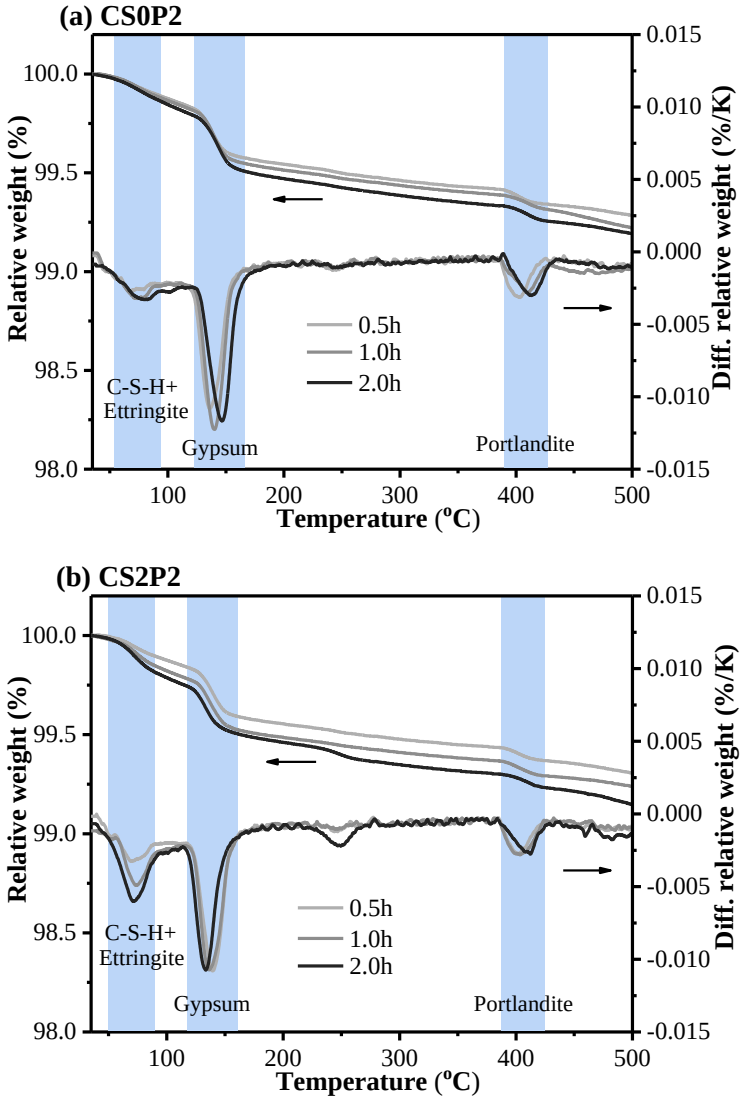

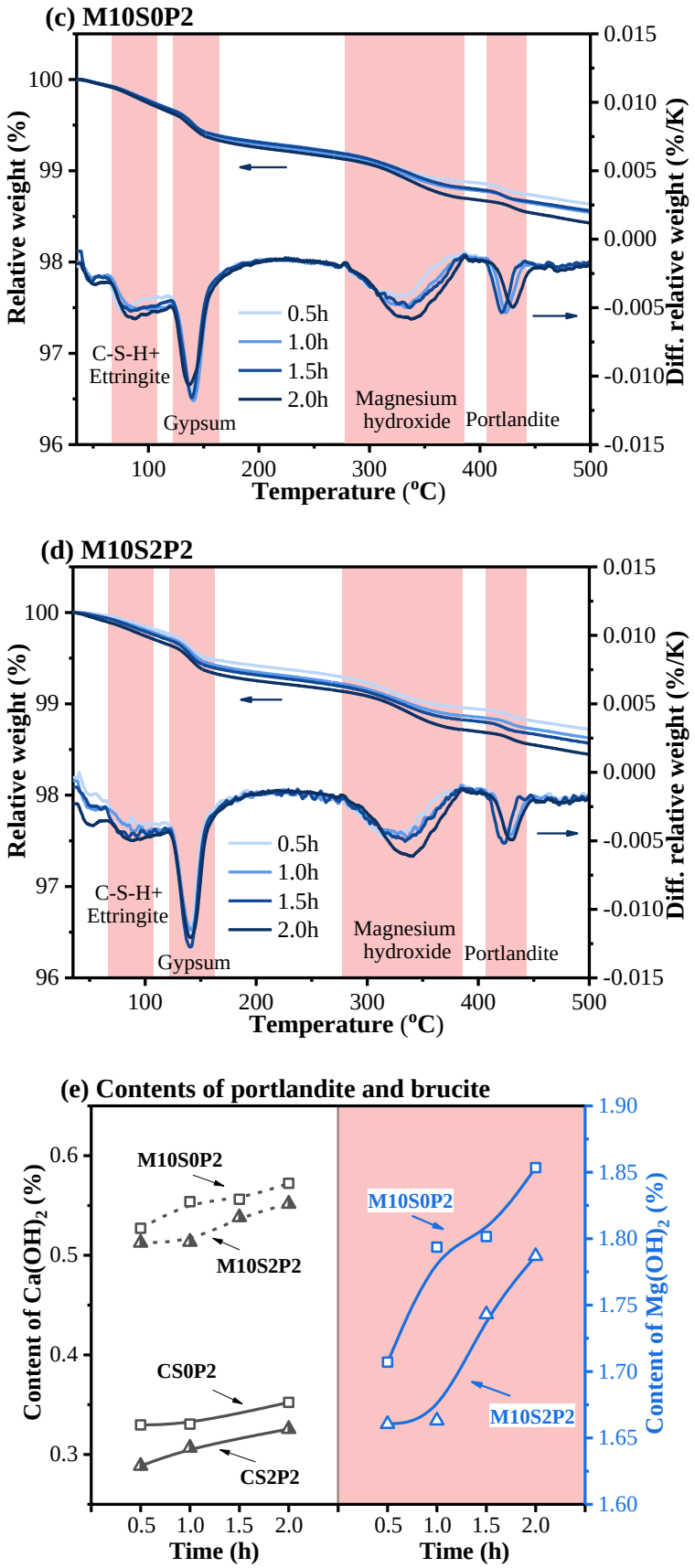


Fig. 10 TGA results of the hydrated blends of LHC and MEA with/without SRA

3.2.3 Zeta potential of re-dispersed suspensions

Fig. 11 shows zeta potential values of re-dispersed suspensions of powder samples hydrating for

different ages with the W/P ratio of 50. Generally, the measurement of Zeta potential is conducted on the diluted suspensions to ensure the test precision. However, the hydration process of cement in the diluted suspensions is far different from the actual condition

Zeta potential values of the four samples are all positive. For CS0P2, the zeta potential value increases first and then decreases with the elapsed time. As reported by Huang et al. [42], the zeta potential of particles from alite paste shows a similar trend with results in this paper, the authors found that the CSH fraction in the solid phase is linearly related with the reduction of zeta potential values because of the deprotonation of surface silanol groups [55]. In M10S0P2, the zeta potential also increases first then decreases with time. However, adding SRA changes it into a basically inverse trend. Doubtlessly, the results confirm that SRA notably changes the surface characteristic of particles in hydrated blends, this seems to be the reason for the dramatical variation of the static yield stress.

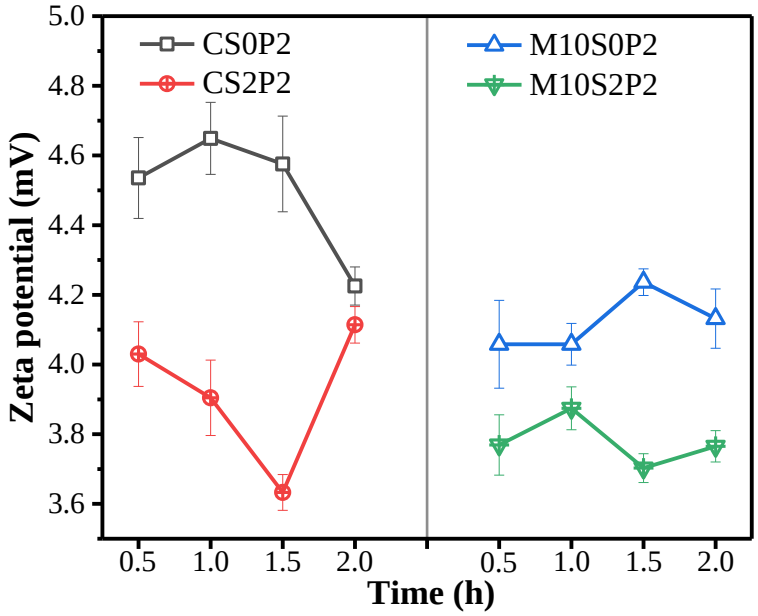


Fig. 11 Zeta potential values of re-dispersed suspensions at W/P ratio of 50

3.2.4 Microstructure morphology of hydrated blends

As seen in previous sections, one of the main hydration products, $Mg(OH)_2$, in LHC-MEA blends makes it more evident to find the correlation between the evolution of static yield stress and the hydrates amount. Results as shown in Fig. 10e confirm that SRA retards the reaction of MgO, however, promotes the static yield stress development of blends even though the hydrate amount is lower. To better understand the effect of SRA on the hydration of blends, especially for the formation of hydrates on the particle surface, SEM observation and BET analysis on hydrated blends were conducted.

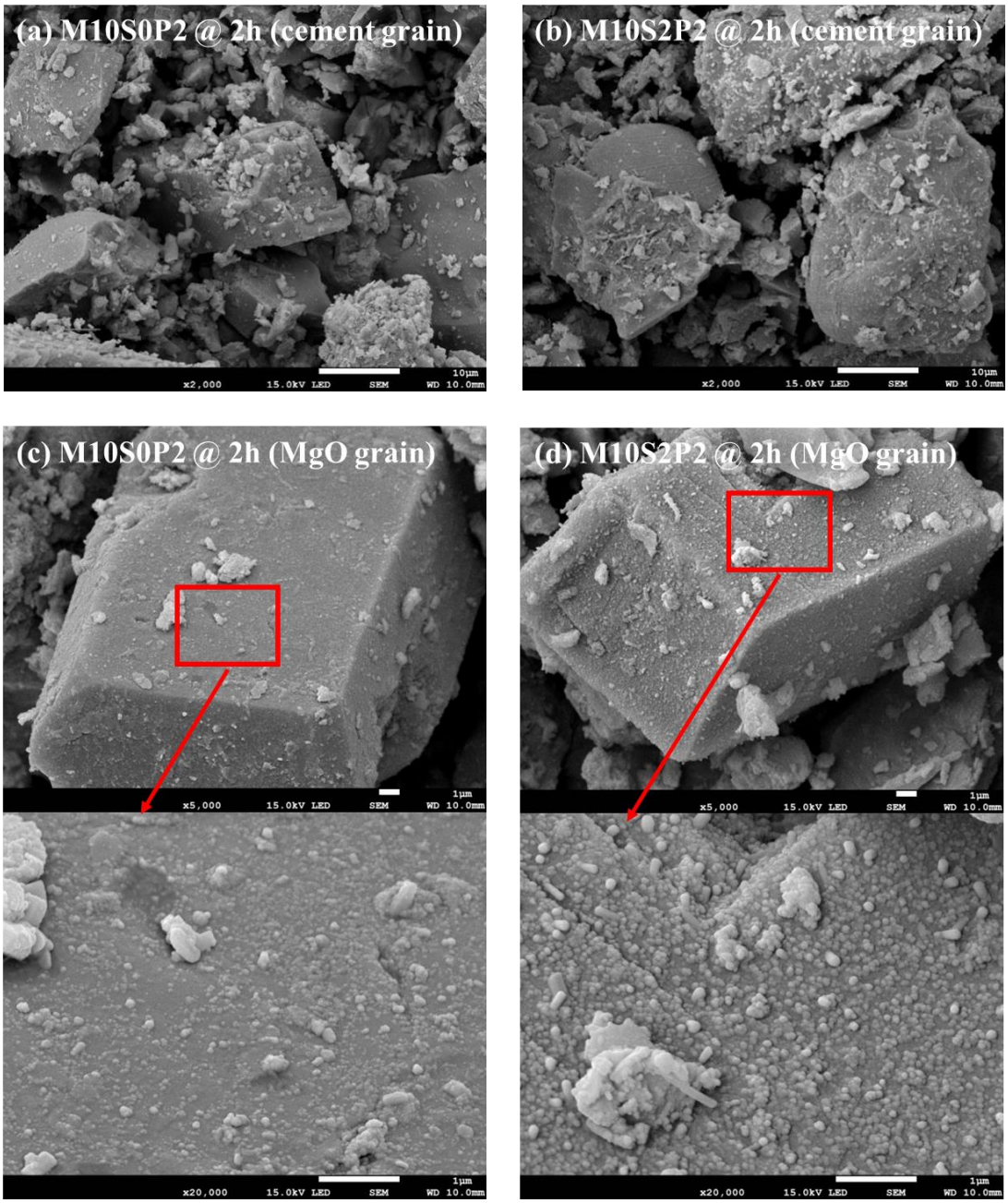


Fig. 12 SEM images of blends of LHC and MEA

Fig. 12 displays the SEM images of hydrated blends, where Fig. 12a and b correspond to cement grains of M10S0P2 and M10S2P2 hydrating for 2h, while Fig. 12c and d are referred to MgO grains of M10S0P2 and M10S2P2 hydrating for 2h. The cement grain surfaces are rough and covered with small-size hydrates. However, it is very hard to distinguish the effect of SRA on hydrate morphology. As seen in Fig. 12c and d, small brucite crystals grow on the surface of MgO grains. As to M10S2P2, the morphologies of the MgO surface at 2h are significantly changed with the addition of 2% SRA. More nucleation sites can be observed in Fig. 12d, where the MgO grain surface is covered with many small-size brucite crystals. A similar phenomenon with the hydrate morphology change has also been reported in [56], with the addition of SRA, finer crystals of hydration products are observed in

ordinary Portland cement system. As seen in the figure, MgO particles in M10S2P2 are covered with more and denser fine brucite crystals, and the particle interactions among sloid particles are strengthened, thus increasing the growth rate of static yield stress.

Table 5 presents the specific surface area of hydrated blends and the corresponding static rheological parameters. With the addition of 10% MEA, the specific surface area of LHC paste is increased from 0.856 $m^2/g$ to 1.5707 $m^2/g$., while the addition of SRA increases the specific surface area of both LHC paste and LHC-MEA blends. There is a clear positive relationship between the surface area and peak value, growth rate of static yield stress. Lou et al. [44] pointed out that cement with a higher hydration rate dissolves more quickly, which reduces the mean particle size and produces pores, thereby increasing the specific surface area. In this paper, the difference between CS0P2 and M10S0P2 in the surface area well correspond to their difference in hydration rate. MEA promotes the hydration of LHC-MEA blends and leads to a higher specific surface area. SRA retards the hydration process, however, contributes to more nucleation sites and amount of brucite crystals on the MgO surface, thereby producing a rougher surface and increasing the specific surface areas of CS2P2 and M10S2P2. The rougher surface contributes to stronger particle interactions and leads to faster static yield stress development.

Table 5 Effect of admixture on the specific surface area of hydrated cement pastes

| Sample at 2h | Surface area of cement paste ($m^2/g$) | Evolution of static yield stress | |
|---|---|---|---|
| | | Peak value (Pa) | Growth rate (Pa/min) |
| CS0P2 | 0.8560 | 105.0 | 0.90 |
| CS2P2 | 0.9671 | 120.3 | 0.93 |
| M10S0P2 | 1.5707 | 176.0 | 1.42 |
| M10S2P2 | 1.5935 | 245.0 | 1.99 |

Based on the results above, the effects of MEA and SRA on the time-dependent behaviour of LHC pastes can be summarised. The hydration of MgO is a typical process of dissolution and crystallization. MgO first dissolves and diffuses into the pore solution and forms the oversaturated solution. Then the formation of $Mg(OH)_2$ takes place at nucleation sites near the MgO grains, such as the MgO grain surface, boundary, and inner pores. The whole hydration process is seen as the self-expansion of MEA particles [3]. Due to the effect of alkali, the size of $Mg(OH)_2$ hydrating in cement pore solution is smaller and more irregular than in pure water [57]. Also, the oversaturation, the sites of nucleation and growth, and the morphology of $Mg(OH)_2$ are reported to be affected by alkali [58].

SRA changes the physicochemical properties of the pore solution in the cement paste and may alter the dissolution and crystallization process of periclase. As shown in Figs. 8-12, SRA retards the hydration of LHC and MEA blends, changes the surface charge of hydrated particles, and reduces the formation contents of $Ca(OH)_2$ as well as $Mg(OH)_2$. Some researchers have summarized the retarding mechanisms of SRA as follows: (i) an organic molecule film is formed by SRA molecules and reduces the interfacial energy, thus hindering the hydration process [59]; (ii) based on the theory of ‘‘similarity and intermiscibility”, SRA reduces the polarity, as well as alkali contents and pH value, of the pore solution and increases the oversaturation level [60, 61]. After mixing with the solution of water and SRA, LHC and MEA grains, due to the polarity, are wetting and wrapped with a water film. Then the SRA molecules adsorb on the surface. The oversaturation level in the pore solution is first reached near the grain surface, however, affected by SRA. Taking MgO as an example, because of the SRA concentration in the pore solution, $Mg(OH)_2$ is prone to nucleating on the MgO surface rather than in the boundary and inner pores. More nucleation sites appear on the surface compared with blends with no SRA, but the total amount of $Mg(OH)_2$ is lower. The amount and morphology of hydrates on grains surface also play an important role in the time-dependent rheological behaviours.

## 4 Conclusions

Based on the experimental data, the main conclusions can be drawn as follows:

(1) The complex interactions among MEA, SRA, and SP on the dynamic yield stress and plastic viscosity are presented by the response surface methodology. The effect of SRA is dependent on the dosage, while the addition of MEA changes the role of SRA on the dynamic yield stress. The zeta potential tests with designed premixing procedures show no evident competitive adsorption between SRA and SP. With the increasing dosage of SRA, the roles of SP and SRA are explained by “adsorbing polymer” and “nonadsorbing polymer”.

(2) The quantitative analysis of hydrate amount is related to the static rheological parameters. MEA increases the growth rate and peak value of the static yield stress in LHC paste for accelerating the early-age hydration of LHC. The content of $Mg(OH)_2$ is higher than other hydrates of LHC. The acceleration effect of MEA on hydration and the formation of $Mg(OH)_2$ both contribute to the static yield stress development.

(3) SRA increases the growth rate and peak value of the static yield stress in both LHC paste and blend of LHC and MEA. At the early-age stage, SRA retards the hydration process of LHC and MEA, leading to lower contents of $Mg(OH)_2$ and $Ca(OH)_2$. The effect of SRA on time-dependent rheological

behaviours stems from changes in the surface charge of hydrated particles and the hydrate morphology on the particle surface.

(4) Taking the content and morphology of $Mg(OH)_2$ as a probe, it is confirmed that hydrates amount is not the only factor affecting the static yield stress development. SRA alters the morphology of brucite and changes the surface charge in hydrated blends of MEA and LHC. More and finer brucite crystals forming on the MgO surface increase the specific surface area and strengthen the particles' interactions, thereby promoting the static yield stress development.

(5) The combined use of MEA and SRA in LHC paste equilibrates the early-age hydration rate, however, makes against the initial flowability. The rheological approach shows the potential for designing the anti-crack concrete with multiple admixtures by taking the workability and the strength gain at rest into consideration.

Nevertheless, only the dosage of SRA is taken into consideration in this paper. It is worth noting that various SRAs with different functional groups and molecule structures may lead to different results on the rheological behaviours and early-age hydration of cement pastes. Therefore, more in-depth investigations are needed on this topic.

**Acknowledgments**

Financial supports by National Natural Science Foundation of China (grant Nos. 51778629 and 51922109), and Innovation-Driven Project of Central South University (grant No. 2020CX011) are greatly acknowledged.

**References**

[1] L. Li, Y. Jin, Y. Jia, et al., Influence of inclusion rigidity on shrinkage induced micro-cracking of cementitious materials, Cem. Concr. Compos. 114(2020) 103773.

[2] China Concrete Cement-based Products Association, "The 13th Five-year Plan" in concrete and cement products industry. 2017.

[3] R.D. Hooton, Future directions for design, specification, testing, and construction of durable concrete structures, Cem. Concr. Res. 124(2019) 105827.

[4] L. Wang, H. Wang, Y. Dong, et al., Environmental evaluation, hydration, pore structure, volume deformation and abrasion resistance of low heat Portland (LHP) cement-based materials, J. Cleaner Prod. 203 (2018) 540-558.

[5] L. Mo, M. Deng, M, Tang, A. Altabbaa, MgO expansive cement and concrete in China: Past, present and future, Cem. Concr. Res. 57(2014) 1-12.

[6] P. Zhan, Z. He, Application of shrinkage reducing admixture in concrete: A review, Constr. Build. Mater. 201(2019) 676-690.

[7] H. Zhang, L. Li, W. Wang, et al., Effect of temperature rising inhibitor on expansion behavior of cement paste containing expansive agent, Constr. Build. Mater. 199(2019) 234-243.

[8] Y. Gu, Z. Wei, Q. Ran, et al., Characterizing cement paste containing SRA modified nano$SiO_2$ and evaluating its strength development and shrinkage behavior, Cem. Concr. Compos. 75(2017) 30-37.

[9] Y. Dang, J. Qian, Y. Qu, et al., Curing cement concrete by using shrinkage reducing admixture and curing compound, Constr. Build. Mater. 48(2013) 992-997.

[10] L. Wang, H. Yang, S. Zhou, et al., Hydration, mechanical property and C-S-H structure of early-strength low-heat cement-based materials, Mater. Lett. 217 (2018) 151-154.

[11] L. Wang, Y. Dong, S. Zhou, et al., Energy saving benefit, mechanical performance, volume stabilities, hydration properties and products of low heat cement-based materials, Energy Build. 170 (2018) 157-169.

[12] F. Dalas, A. Nonat, S. Pourchet, et al., Tailoring the anionic function and the side chains of comb-like superplasticizers to improve their adsorption, Cem. Concr. Res. 67 (2015) 21-30.

[13] X. Ouyang, Y. Guo, X. Qiu, The feasibility of synthetic surfactant as an air entraining agent for the cement matrix, Constr. Build. Mater. 22(2008) 1774-1779.

[14] L. Ferrari, J. Kaufmann, F. Winnefeld, J. Plank, Interaction of cement model systems with superplasticizers investigated by atomic force microscopy, zeta potential, and adsorption measurements, J. Colloid Interface Sci. 347 (2010) 15-24.

[15] K. Matsuzawa, D. Atarashi, M. Miyauchi, E. Sakai, Interactions between fluoride ions and cement paste containing superplasticizer, Cem. Concr. Res. 91 (2017) 33-38.

[16] J. Plank, C. Winter, Competitive adsorption between superplasticizer and retarder molecules on mineral binder surface, Cem. Concr. Res. 38(5)(2008) 599-605.

[17] I. Mehdipour, K.H. Khayat, Effect of shrinkage reducing admixture on early expansion and strength evolution of calcium sulfoaluminate blended cement, Cem. Concr. Compos. 92(2018) 82-91.

[18] F. Tittarelli, C. Giosuè, S. Monosi, Combined use of shrinkage reducing admixture and CaO in cement based materials, IOP Conf. Ser. Mater. Sci. Eng. 245(2017) 022093.

[19] M.J. Oliveira, A.B. Ribeiro, F.G. Branco, Combined effect of expansive and shrinkage reducing admixtures to control autogenous shrinkage in self-compacting concrete, Constr. Build. Mater.

52(2014) 267-275.

[20] Z. He, Z. Li, M. Chen, W. Liang, Properties of shrinkage-reducing admixture-modified pastes and mortar, Mater. Struct. 39(4)(2005) 445-453.

[21] F. Rajabipour, G. Sant, J. Weiss, Interactions between shrinkage reducing admixtures (SRA) and cement paste's pore solution, Cem. Concr. Res. 38(5)(2008) 606-615.

[22] J.J. Brooks, M.A.M. Johari, M. Mazloom, Effect of admixtures on the setting times of high-strength concrete, Cem. Concr. Compos. 22(4)(2000) 293-301.

[23] S. Monosi, R. Troli, O. Favoni, F. Tittarelli, Effect of SRA on the expansive behaviour of mortars based on sulphoaluminate agent, Cem. Concr. Compos. 33(4)(2011) 485-489.

[24] D. Jiao, C. Shi, Q. Yuan, et al., Effect of constituents on rheological properties of fresh concrete-A review, Cem. Concr. Compos. 83(2017) 146-159.

[25] K. Han, J. Xiao, Z. Zhang, et al., Effect of particle size distribution on flocculation and its growth in cement-ground limestone suspensions, Constr. Build. Mater. 262(2020) 120047.

[26] F. Mahaut, S. Mokéddem, X. Chateau, N. Roussel, G. Ovarlez, Effect of coarse particle volume fraction on the yield stress and thixotropy of cementious materials, Cem. Concr. Res. 38(11)(2008) 1276-1285.

[27] H. Bessaies-Bey, R. Baumann, M. Schmitz, M. Radler, N. Roussel, Organic admixtures and cement particles: Competitive adsorption and its macroscopic rheological consequences, Cem. Concr. Res. 80 (2016) 1-9.

[28] B. Wu, B. Chun, L. Gu, T. L. Kuhl, Adsorption properties of poly(carboxylate ether) to negatively charged surfaces in high-salt conditions, Cem. Concr. Res. 118(2019) 102-110.

[29] J. Hot, H. Bessaiesbey, C. Brumaud, et al., Adsorbing polymers and viscosity of cement pastes, Cem. Concr. Res. 2014(63) 12-19.

[30] F. Cao, M. Miao, P. Yan, Effects of reactivity of MgO expansive agent on its performance in cement-based materials and an improvement of the evaluating method of MEA reactivity, Constr. Build. Mater. 187(2018) 257-266.

[31] L. Mo, M. Deng, M. Tang, Effects of calcination condition on expansion property of MgO-type expansive agent used in cement-based materials, Cem. Concr. Res. 40(3)(2010) 437-446.

[32] R. Zhang, D.K. Panesar, New approach to calculate water film thickness and the correlation to the rheology of mortar and concrete containing reactive MgO, Constr. Build. Mater. 150(2017) 892-902.

[33] D. Yoo, N. Banthia, Y. Yoon, Effectiveness of shrinkage-reducing admixture in reducing autogenous shrinkage stress of ultra-high-performance fiber-reinforced concrete, Cem. Concr. Compos. 64(2015) 27-36.

[34] J. Han, H. Fang, K. Wang, Design and control shrinkage behavior of high-strength self-consolidating concrete using shrinkage-reducing admixture and super-absorbent polymer, J. Sustainable. Cem. Mater. 3(3-4)(2014) 182-190.

[35] N. Roussel, G. Ovarlez, S. Garrault, et al., The origins of thixotropy of fresh cement pastes, Cem. Concr. Res. 42 (2012) 148-157.

[36] I. Ferdosian, A. Camões, Eco-efficient ultra-high performance concrete development by means of response surface methodology, Cem. Concr. Compos. 84(2017) 146-156.

[37] GB/T 200-2017, Moderate-heat Portland cement, low-heat Portland cement (in Chinese).

[38] T/CECS 540-2018, Technical specification for application of MgO expansive agent for concrete (in Chinese).

[39] T. Huang, B. Li, Q. Yuan, et al., Rheological behavior of Portland clinker-calcium sulphoaluminate clinker-anhydrite ternary blend. Cem. Concr. Compos. 104(2019) 103403.

[40] Q. Yuan, D. Zhou, K. H. Khayat, et al., On the measurement of evolution of structural build-up of cement paste with time by static yield stress test vs. small amplitude oscillatory shear test, Cem. Concr. Res. 99(2017) 183-189.

[41] Q. Yuan, D. Zhou, B. Li, et al., Effect of mineral admixtures on the structural build-up of cement paste, Constr. Build. Mater. 160(2018) 117-126.

[42] T. Huang, Q. Yuan, F. He, et al., Understanding the mechanisms behind the time-dependent viscoelasticity, Cem. Concr. Res. 133 (2020) 106084.

[43] H.V. Daake, D. Stephan, Adsorption kinetics of retarding admixtures on cement with time controlled addition, Cem. Concr. Res. 102 (2017) 119-126.

[44] H. Lou, K. Ji, H. Lin, et al., Effect of molecular weight of sulphonated acetone-ormaldehyde condensate on its adsorption and dispersion properties in cementitious system, Cem. Concr. Res. 42 (2012) 1043-1048.

[45] R.W. O'Brien, D.W. Cannon, W.N. Rowlands, Electroacoustic Determination of Particle Size and Zeta Potential, J. Colloid Interface Sci. 173(2)(1995) 406-418.

[46] D. Lowke, Thixotropy of SCC—A model describing the effect of particle packing and superplasticizer adsorption on thixotropic structural build-up of the mortar phase based on

interparticle interactions, Cem. Concr. Res. 104 (2018) 94-104.

[47] H. Bessaies-Beya, M. Palacios, E. Pustovgar, et al., Non-adsorbing polymers and yield stress of cement paste, Cem. Concr. Res. 111 (2018) 209-217.

[48] Q. Yuan, X. Lu, K. H. Khayat, et al., Small amplitude oscillatory shear technique to evaluate structural build-up of cement paste, Mater. Struct. 50(2)(2017) 1-12.

[49] R. A. Buswell, W. R. Leal De Silva, S. Z. Jones, et al., 3D printing using concrete extrusion: A roadmap for research, Cem. Concr. Res. 112(2018) 37-49.

[50] L. Reiter, T. Wangler, N. Roussel, et al., The role of early age structural build-up in digital fabrication with concrete, Cem. Concr. Res. 112 (2018) 86-95.

[51] A.F. Omran, K.H. Khayat, Choice of thixotropic index to evaluate formwork pressure characteristics of self-consolidating concrete, Cem. Concr. Res. 63(2014) 89-97.

[52] N. Roussel, F. Cussigh, Distinct-layer casting of SCC: The mechanical consequences of thixotropy, Cem. Concr. Res. 38(5)(2008) 624-632.

[53] L. Leonreina, A. G. La Torre, J. M. Porrasvazquez, et al., Round robin on Rietveld quantitative phase analysis of Portland cements, J. Appl. Crystallogr. 42(5)(2009) 906-916.

[54] T. Huang, Q.Yuan, S. Zuo, et al., Evolution of elastic behavior of alite paste at early hydration stages, J. Am. Ceram. Soc. https://doi.org/10.1111/jace.17354.

[55] H. Viallisterrisse, A. Nonat, J.C. Petit, Zeta-Potential Study of Calcium Silicate Hydrates Interacting with Alkaline Cations, J. Colloid Interface Sci. 244(1)(2001) 58-65.

[56] S. Monosi, R. Troli, O. Favoni, et al., Effect of SRA on the expansive behaviour of mortars based on sulphoaluminate agent, Cem. Concr. Compos. 33(4)(2011) 485-489.

[57] L. Mo, M. Deng, M. Tang, Effects of calcination condition on expansion property of MgO-type expansive agent used in cement-based materials, Cem. Concr. Res. 40(3)(2010) 437-446.

[58] J. Lv, L. Qiu, B. Qu, Controlled growth of three morphological structures of magnesium hydroxide nanoparticles by wet precipitation method, J. Cryst. Growth. 267(3-4)(2004) 676-684.

[59] Y. Wehbe, A. Ghahremaninezhad, Combined effect of shrinkage reducing admixtures (SRA) and superabsorbent polymers (SAP) on the autogenous shrinkage, hydration and properties of cementitious materials, Constr. Build. Mater. 138(2017) 151-162.

[60] G. Santa, B. Lothenbach, P. Juilland, et al., The origin of early age expansions induced in cementitious materials containing shrinkage reducing admixtures, Cem. Concr. Res. 41(3)(2011) 218-229.

[61] W. Zuo, P. Feng, P, Zhong, et al., Effects of novel polymer-type shrinkage-reducing admixture on early age autogenous deformation of cement pastes, Cem. Concr. Res. 100(2017) 413-422.